



1 **Influence of crustal mechanical layering on the seismic potential of active**
2 **faults: insights from the southwestern Valencia Trough (W Mediterranean)**

3

4 Martin-Rojas, Iván¹

5 Ramos, Adriá¹

6 De Ruig, Menno²

7 Medina-Cascales, Iván¹

8 Santamaría-Pérez, Eva¹

9 Alfaro, Pedro¹

10

11 1 Dpto. de Ciencias de la Tierra y del Medio Ambiente, Universidad de Alicante,

12 Campus San Vicente s/n, 03690, San Vicente del Raspeig, Alicante.

13 ivan.martin@ua.es

14 2. Oropesa BV, Van Bleiswijkstraat 183, 2582 LD The Hague, Netherlands.

15 menno.deruig@gmail.com

16

17 Corresponding author: Martin-Rojas, Iván

18 Dpto. de Ciencias de la Tierra y del Medio Ambiente, Universidad de Alicante,

19 Campus San Vicente s/n, 03690, San Vicente del Raspeig, Alicante.

20 ivan.martin@ua.es

21

22



23 **Short summary**

24 This study investigates the main active faults located within the southwestern
25 Valencia Trough, an offshore region east of the Spanish coast. Utilizing subsurface
26 data, we identify and characterize the 3D geometry of several of these faults for the
27 first time. Given that active faults pose a significant natural hazard due to their
28 potential to generate earthquakes, we also assess the seismic potential of the faults
29 within the southwestern Valencia Trough.

30



31 **ABSTRACT**

32

33 We present a structural and seismotectonic analysis of active faults in the
34 southwestern Valencia Trough (western Mediterranean) on the basis of subsurface
35 datasets. In our study, we identify and characterise three major active faults: the
36 Cullera Fault, with a long-term slip rates that vary over time between 0.15 ± 0.1
37 mm/yr and 0.4 ± 0.1 mm/yr; the oblique Albufera Fault, with a long-term slip rate of
38 0.2 ± 0.1 mm/yr; and the normal Valencia Fault.

39 The seismogenic character of the southwestern Valencia Trough is controlled by a
40 mechanically weak layer consisting of Triassic evaporites. This weak layer induces
41 partial to complete decoupling between the suprasalt and subsalt successions,
42 leading to two distinct mechanisms driving fault displacement: tectonic activity and
43 salt withdrawal. A quantitative evolutionary analysis of the Cullera Fault reveals that
44 these two mechanisms alternate over time.

45 The presence of a mechanically weak layer has implications for seismicity.
46 Earthquakes can nucleate within both sub- and suprasalt successions, with total or
47 partial decoupling influencing rupture propagation. We discuss how these two
48 scenarios lead to different earthquakes and thus impact the seismic hazard of a
49 region. Empirical source-scaling relationships, which are commonly used to
50 estimate the seismogenic potential of active faults, generally assume a
51 homogeneous seismogenic crust. To address this limitation, we propose a
52 methodological approach based on the use of the aspect ratio. Our findings
53 highlight the need to incorporate stratigraphic mechanical layering into seismic

54 hazard assessments, particularly in salt-influenced tectonic settings.



55

56



57 **1. Introduction**

58 Seismic-hazard analyses are often performed by scaling relationships. These
59 relationships are regressions in which the seismogenic potential of active faults is
60 derived from geometric parameters of the fault, such as the potential fault rupture
61 length or area (Stirling et al., 2013). Pioneering works on scaling relationships began
62 in the 1970s (Kanamori & Anderson, 1975; Geller, 1976). The regressions of Wells &
63 Coppersmith (1994) represent a milestone in the application of scaling
64 relationships, as they included a very large dataset of historical earthquakes. The
65 equations proposed by Wells & Coppersmith became a standard for determining
66 the seismogenic potential of active faults. Subsequently, other scaling relationships
67 have been proposed, accounting for factors such as the tectonic environment, fault
68 dip, or seismogenic thickness (Stirling et al., 2002 and 2013; Leonard 2010 and
69 2014; Huang et al., 2024, among many others).

70 Most scaling relationships employed to evaluate crustal earthquakes correlate the
71 moment magnitude (M_w) with the fault dimensions (length, width, and/or area).
72 Some of these scaling relationships consider the fault width vs. fault dip growth of
73 ruptures for large earthquakes, as rupture width is limited by the maximum depth of
74 the seismogenic crust (Leonard, 2010; Yen and Ma, 2011; Leonard, 2014; Cheng et
75 al., 2019). However, these relationships do not consider the influence of potential
76 heterogeneities within the seismogenic crust, which could control the propagation
77 of ruptures and, therefore, the magnitude of earthquakes.

78 Here, we present an analysis of several subsurface datasets, including high-
79 resolution seismic profiles, from the southwestern Valencia Trough. We identify and
80 characterise the main active faults in this region, and we carry out a detailed
81 geometric description. The results of this analysis also emphasize that this region is
82 characterised by a mechanically weak layer within the seismogenic crust. After
83 mapping the main faults, we apply conventional scaling relationships to evaluate
84 the potential magnitudes of future earthquakes. We propose a methodological
85 approach for integrating the effects of mechanically weak layers—such as Triassic
86 evaporites—into routine seismic hazard assessments, highlighting the need to
87 refine existing scaling relationships in tectonically complex settings.



88 2. Tectonic setting

89 The Valencia Trough is an extensional basin located in the western Mediterranean
90 region (Fig. 1). This basin is the result of polyphase tectonic evolution spanning from
91 the Triassic to the present day, as it is located between the Betic-Balearic fold-and-
92 thrust belt to the south, the Iberian Chain to the west, and the Catalan Coastal
93 Ranges to the north (De Ruig, 1992; Guimerà & Álvaro, 1990; Maillard & Mauffret,
94 1999; Roca & Desegaulx, 1992; Roca et al., 2004; Vergés & Fernández, 2012). The
95 tectonic evolution of the Valencia Trough is also partially influenced by extension
96 related to the retreat of the Maghrebian–Ligurian Tethys subduction slab (Etheve et
97 al., 2016; Faccenna et al., 2004; Jolivet & Faccenna, 2000; Maillard & Mauffret, 1999;
98 Rehault et al., 1984; Roca et al., 1999; Séranne, 1999; van Hinsbergen et al., 2014).

99 The Valencia Trough (Fig. 1) underwent a Mesozoic rifting process related to the
100 Iberian intraplate rift and the opening of the Western Tethys (Arche and López-
101 Gómez, 1996; Nebot and Guimerà, 2018; Ramos et al., 2023; Salas et al., 2001). This
102 process led to the formation of NW–SE and NE–SW high-angle faults offsetting the
103 pre-Mesozoic basement and to the deposition of a 5–15-km-thick Upper Jurassic–
104 Lower Cretaceous succession.

105 During the Late Cretaceous, the onset of convergence between Nubia and Eurasia
106 caused the transition from a Mesozoic extensional tectonic regime to successive
107 compressional and extensional stages (Roca, 2001; Salas et al., 2001; Vergés and
108 Sàbat, 1999). From the late Eocene to the Oligocene, the Valencia Trough was
109 dominated by shortening. Onshore, this episode led to the formation of the
110 intraplate Iberian Chain and Catalan Coastal Ranges (Gaspar-Escribano et al.,
111 2004; Geel, 1995; Guimerà and Álvaro, 1990).

112 From the late Oligocene to the middle Miocene, the western Mediterranean region
113 was subsequently affected by an extensional regime, driven by the complex
114 interplay between the European–Cenozoic rift system (e.g., Séranne, 1999) and the
115 rollback of the Maghrebian–Ligurian Tethys slab (Faccenna et al., 2004; van
116 Hinsbergen et al., 2014). This extensional phase led to the formation of the Liguro-
117 Provençal and Algerian Basins, as well as the Valencia Trough. However, subsidence
118 in the southwestern Valencia Trough during this period cannot be accounted for by





119 rifting, due to the limited occurrence of Cenozoic basement extensional faults
120 (Roca and Guimerà, 1992). Therefore, extension has been interpreted as due to the
121 collapse of a back-arc transient uplift event (Fang et al., 2021).

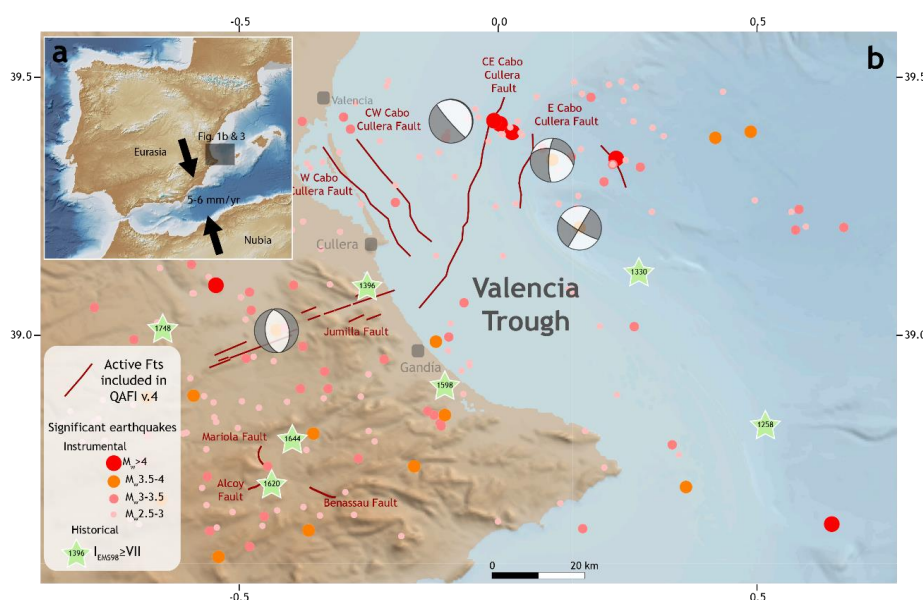
122 The extension in the Valencia Trough occurred immediately before or synchronously
123 with the formation of the compressional Betic Cordillera. This compressional
124 deformation is well expressed by a thin-skinned fold-and-thrust system observed in
125 the Eastern Betic Cordillera (De Ruig, 1995; Sàbat et al., 2011) and in the Balearic
126 Promontory (Mallorca and Ibiza Islands). At the same time, significant magmatic
127 activity took place in the area, and was divided into two phases: (1) late Oligocene
128 to Serravallian calc-alkaline activity and (2) Tortonian to present alkaline volcanic
129 activity (Martí et al., 1992).

130 From the Pliocene to the present, the tectonic setting in the Valencia Trough has
131 been dominated by NE–SW extension, as indicated by focal mechanisms (Stich et
132 al., 2010) and broad regional global navigation satellite system (GNSS) analyses
133 (Stich et al., 2006). This extension has been related to thermal subsidence (Roca,
134 1992, 1996, and 2001; Roca and Guimerà, 1992; Roca et al., 1999a; Gaspar-
135 Escribano et al., 2004) and has been interpreted as the final stage of an aborted rift
136 event responsible for the ENE motion of the Balearic promontory (Palano et al.,
137 2015). Several normal active faults have been defined in the southwestern Valencia
138 Trough thus far (Fig. 1): the Western Cabo Cullera Fault, Central–Western Cabo
139 Cullera Fault, Central–Eastern Cabo Cullera Fault, Eastern Cabo Cullera Fault and
140 Southwest Columbretes Fault (Perea, 2006). Some of these faults were previously
141 recognised from vintage seismic lines (Díaz del Río et al., 1986; Roca, 1992, 1996;
142 Perea, 2006; Maillard & Mauffret, 2013), but fault traces and geometry were defined
143 only very approximately. Similarly, the slip rates derived from the displacement of
144 Plio-Quaternary seismic reflectors observed in the vintage seismic lines present
145 high uncertainties (0.02 ± 0.01 mm/yr; Perea, 2006). In the Valencia Trough,
146 seismicity is characterised by low- to moderate-magnitude events (Fig. 1). The few
147 available focal mechanisms (Stich et al., 2010; IGN, 2025) indicate a normal–
148 oblique or strike slip kinematics, although these focal mechanisms present high
149 uncertainties, mainly because they occur at long distances from seismic stations



150 and are registered with significant azimuthal gaps (González, 2017). According to
151 the data published by the Spanish Earthquake Catalogue (IGN, 2025), this
152 seismicity is very shallow, as most of the events are assigned depths of less than 10
153 km (Fig. 2). However, ~~once again~~, these data should be taken with caution, as the
154 depths assigned to these earthquakes present high uncertainties (González, 2017).

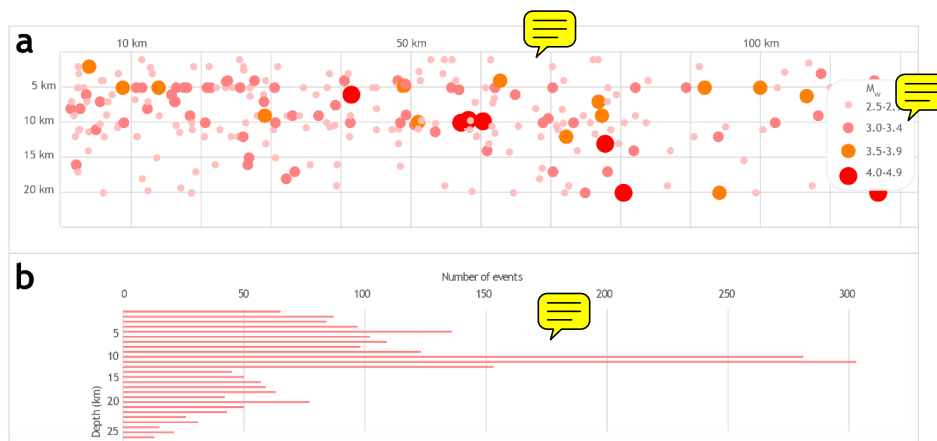
155 In the onshore domain located west of the Valencia Trough, only one major active
156 structure, namely, the Jumilla Fault, has been postulated (García-Mayordomo et al.,
157 2012), together with other minor active faults (Alcoy, Mariola, and Benasau Faults).
158 In this onshore area, several significant historical earthquakes have occurred, such
159 as the 1396 Tavernes ($I_{EMS98}=VIII-IX$), 1620 Alcoy ($I_{EMS98}=VIII-IX$), 1644 Muro ($I_{EMS98}=V$)
160 and 1748 Estubeny ($I_{EMS98}=IX$) earthquakes (Martínez Solares and Mezcua, 2002;
161 IGN, 2025; Bufo et al., 2010; Bufo & Udías, 2022).



162
163 Fig. 1. a. Location of the Valencia Trough. Convergence vectors between Nubia and
164 Eurasia are after DeMets et al., 1994; McClusky et al., 2003; Nocquet, 2012;
165 Nocquet & Calais, 2003; Pérez-Peña et al., 2010; Serpelloni et al., 2007; Stich et al.,
166 2006. b. Seismotectonic map of the southwestern Valencia Trough and surrounding
167 areas. Fault traces from Quaternary-Active Faults of Iberia database (García-
168 Mayordomo et al., 2012)



169



170

171 Fig 2. Seismicity of $M_w > 2.5$ in the southwestern Valencia Trough shallower than 20
 172 km since 1950 from the Instituto Geográfico Nacional database (IGN, 2025) a.
 173 Distribution of the depth of seismicity. Horizontal axis represents distance along the
 174 southwestern Valencia Trough in a SW-NE direction. b. Depth histogram.



175 **3. Methods**

176 The interpretation of the offshore area is based on mainly 2D multichannel seismic
177 reflection data calibrated with well data (Fig. 3). The central part of the study area is
178 covered by a high-quality seismic survey acquired by Fugro-Geoteam with the RV
179 Geo Baltic, processed by Robertson Research International Ltd. in 2002. The survey
180 consists of 30 seismic sections with an average length of 90 km (totalling
181 approximately 2,800 km). They are oriented WNW–ESE and NNE–SSW, with
182 maximum spacings of 13 km and 6 km, respectively. The details regarding the
183 acquisition and processing parameters can be found in Cameselle & Urgeles (2017).
184 Most of the area affected by Plio-Quaternary faulting nearer to the coast is covered
185 only by vintage 2D seismic lines from the late 1970s, acquired by various operators,
186 which are publicly available upon request in the Instituto Geológico y Minero de
187 España (IGME-CSIC) (<http://info.igme.es/sigeof/>). More than 100 of these seismic
188 lines, with a total line length of approximately 2,500 km, were selected for mapping;
189 although the quality of these lines varies from moderate to poor, the high-density
190 grid spacing (varying from 1 to 3.5 km) allows fault mapping with reasonable
191 confidence. The seismic interpretation was performed in two-way travel time (TWT)
192 by using Move software (by Petex). The seismic dataset was converted to depths
193 using velocity data derived from Expanded Spread Profile ESP 7 (Pascal et al., 1992;
194 Torné et al., 1992). A second-order polynomial trend was applied to establish time–
195 depth relationships, ensuring strong correlation with the well data, similar to the
196 methodologies of Fang et al. (2021).

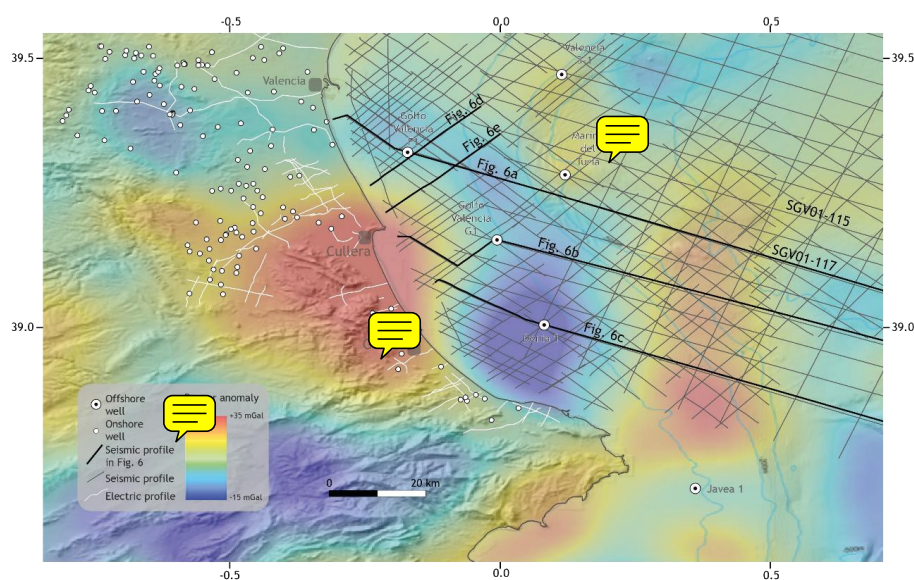
197 The interpretation of seismic horizons is calibrated by 9 offshore petroleum
198 exploration wells, all of which penetrate the entire Neogene section and whose
199 bottoms are in Mesozoic rocks. Original well reports, log data (lithology, dipmeter,
200 gamma–ray, sonic and resistivity data) and palaeontological data (from cuttings and
201 sidewall cores) were retrieved from the IGME-CSIC archive
202 (<https://info.igme.es/hidrocarburos/>). Well-to-seismic ties were established by
203 integrating the sonic logs and using synthetic seismograms from end-of-well
204 reports. Palaeontological analyses and range charts from the original well reports



205 were reviewed and adapted to the Mediterranean biozonation of Lirer et al. (2019) to
206 obtain approximate absolute ages for the seismic horizons.

207 No seismic data were available for the onshore area of southern Valencia and only
208 two deep exploration wells were drilled (Jaraco-1 and Perenchiza-1). However,
209 stratigraphic information is available from 95 hydrogeological wells in the Valencia
210 coastal plain, as are vertical electric sounding (VES) profiles acquired for
211 hydrogeological surveys. The data are publicly available in the online IGME-CSIC
212 databases IRYDA, BD Puntos Agua 2.0 and Sistema de Información Documental
213 (SID) (accessible through <https://info.igme.es/catalogo/>).

214 In areas with poor seismic coverage, structural mapping was aided by regional
215 Bouguer gravity anomalies processed with a Butterworth High-pass filter with a 1-
216 degree cut-off frequency to highlight short-wavelength features of the data (by
217 Getech, 2015).



218
219 Fig. 3. Geophysical dataset used in this work. Filtered Bouguer anomaly data after
220 Getech (2015). The location is shown in figure 1.

221



222 4. Stratigraphy

223 The general stratigraphic arrangement of the southwestern Valencia Trough (Fig. 4)
224 consists of a rigid Palaeozoic–Middle Triassic basement overlain by a 1.5–7-km
225 Upper Triassic–Quaternary stratigraphic cover. Here we present a new detailed
226 stratigraphic framework for the late Miocene–Quaternary of the southern Valencia
227 Trough. The definition of the pre-Neogene stratigraphic units presented in this work
228 is based on mainly previous literature and our analysis of well data, as well as
229 outcrops in the mainland for the most recent sediments.

230 The Upper Triassic succession (Fig. 4) consists of evaporites, shales and dolomites
231 (Keuper Facies) (Vargas et al., 2009). The Upper Triassic deposits are overlain by
232 shallow-water dolomites and anhydrites deposited from the Early to Middle Jurassic
233 (Salas et al., 2001). The Upper Jurassic and Lower Cretaceous successions are
234 represented by platform carbonates that grade to marls basinwards and are overlain
235 by middle–late Albian to Late Cretaceous carbonates. The top of the Mesozoic
236 succession corresponds to an erosive, angular unconformity that is directly overlain
237 by Neogene deposits. Cenozoic infilling has been broadly studied in recent decades
238 (e.g., Arche et al., 2010; Clavell and Berástegui, 1991; Maillard et al., 1992; Ribó et
239 al., 2016b, 2016a; Soler et al., 1983). The succession starts with a transition from
240 continental clastic sediments to marine platform carbonates, ending with a deposit
241 formed by progradational terrigenous shelf-talus sediments (Clavell and
242 Berástegui, 1991; Etheve et al., 2018; Lanaja, 1987; Roca and Desegaulx, 1992;
243 Soler et al., 1986).

244 The Neogene succession onshore of the southwestern Valencia Trough (Fig. 4)
245 mostly consists of middle–late Miocene continental to marginal marine deposits. In
246 the offshore part of the study area, the Miocene stratigraphic succession is entirely
247 marine. The base of the Miocene sequence is composed of a basal conglomerate
248 overlain by coralline algal limestones. The middle Miocene (late Langhian–
249 Serravallian) deep marine calcareous claystones, marls and fine-grained
250 sandstones overlie the algal limestones or rest directly on deeply eroded Mesozoic
251 rocks. Within the southern and central parts of the study area, the early–middle
252 Miocene sequence is no more than 200 m thick. Towards the north, the middle



253 Miocene interval rapidly thickens, reaching almost 2000 m. Tortonian and Messinian
254 deposits consist of mainly marls with thicknesses varying between 180 m and 425
255 m. The top of the Tortonian–Messinian series is an erosional unconformity
256 (Messinian Erosion Surface (MES)) (Stampfli & Höcker, 1989; Lofi et al., 2011;
257 Cameselle et al., 2014).

258 In the onshore and nearshore areas, upper Miocene deposits are overlain by thin
259 cover (generally less than 50 m) of Pleistocene–recent alluvial fans, laterally grading
260 to lagoonal and beach barrier deposits near the coast. No Pliocene sediments have
261 been identified in the entire onshore coastal area, except for local karstic cave infills
262 with mammal remains (Agustí et al., 2011). Below the southern parts of the city of
263 Valencia, the thickness of Pleistocene–recent deposits abruptly increases. Vertical
264 electric sounding profiles seem to indicate the presence of several large normal
265 faults in this area, which have locally dropped the top Miocene surface down to
266 more than 400 m below sea level. From Cullera southwards, shallow boreholes
267 encounter Pleistocene to recent interbedded alluvial gravels, brackish lagoon, and
268 beach barrier deposits. Vertical electric sounding profiles and well correlations
269 indicate abrupt thickness changes, likely controlled by a complex system of normal
270 faults in the Mesozoic–middle Miocene basement, ranging from less than 50 m in
271 offset to more than 200 m towards the coast. Subsidence in the southern Valencian
272 coastal area continues to the present day, as evidenced by well-documented
273 submerged beach barriers of Tyrrhenian age (Eemian interglacial, 127–106ky),
274 which are currently found between 10 and 40 m below sea level in shallow offshore
275 areas (Zazo et al, 1979; Alcántara-Carrió et al, 2012).

276 In the offshore area, Pliocene–recent sediments form a large prograding shelf
277 complex with prominent clinoforms visible in seismic data, which downlap onto the
278 MES. Prominent undulations on slope foresets are visible on most seismic lines and
279 are interpreted as sediment waves (Ribó et al., 2015). In the offshore wells, the
280 stratigraphic succession consists of an overall shallowing-upward series of thick
281 grey claystones with calcareous interbeds at the base, grading upwards into
282 sandstones and shell beds at the top. No unconformities have been identified in the



entire sequence, except for erosional gullies and canyons at the shelf edge. The Plio-Quaternary sequence reaches a maximum thickness of approximately 3000 m.

To determine the Plio-Quaternary depositional history and slip rate of major faults, six seismic horizons have been mapped and dated with palaeontological data from offshore wells, via the biostratigraphic scheme of Lirer et al. (2019). Starting from the Messinian unconformity at 5.3 Ma, seismic markers have been dated at 3.8 Ma (LO of *G. margaritae*), 3.3 Ma (FO *G. bononiensis*), 2.6 Ma (LCO *G. obliquus*) and 2.0 Ma (FO *G. truncatulinoides*). As no samples were collected from any of the offshore wells above the lower-middle Pleistocene interval, an additional marker (approximately 1.0 Ma) has been picked halfway through the 2.0 Ma marker and seabed (0 Ma), assuming a constant sedimentation rate.

Isopach maps (Fig. 5) were produced for the intervals of Pliocene (MES to 2.6 Ma marker) and Pleistocene–recent (2.6 Ma marker to the seabed), revealing a significant shift in the location of the depocenter. The Pliocene depocentre is located very close to the southern coast near Denia, attaining a maximum thickness of approximately 1500 m, whereas the Pleistocene depocentre has prograded ca. 20 km to the NNW, reaching a thickness of more than 1750 m. The western shoreward edge of both the Pliocene and Pleistocene depocentres is controlled by very large NNW–SSE-trending normal faults (see below).

The described stratigraphic architecture indicates significant mechanical layering in the southwestern Valencia Trough. A rigid basement is overlain by a mechanically weak layer represented by the Upper Triassic Keuper Facies. Above this interval, a rigid Mesozoic carbonate succession is present, followed by a semirigid layer composed of primarily detrital deposits.

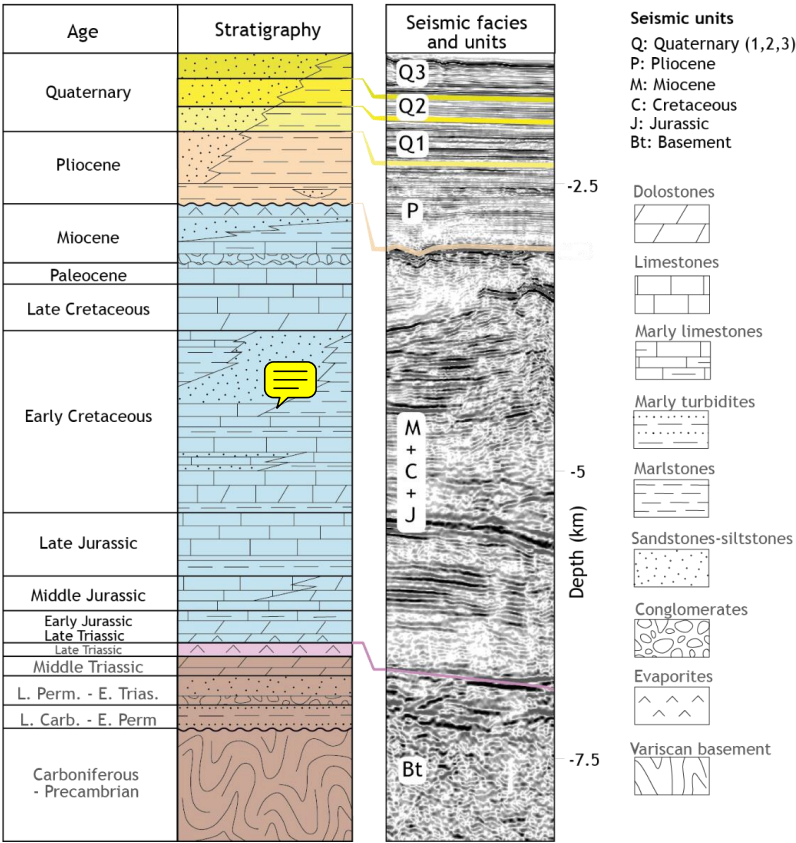
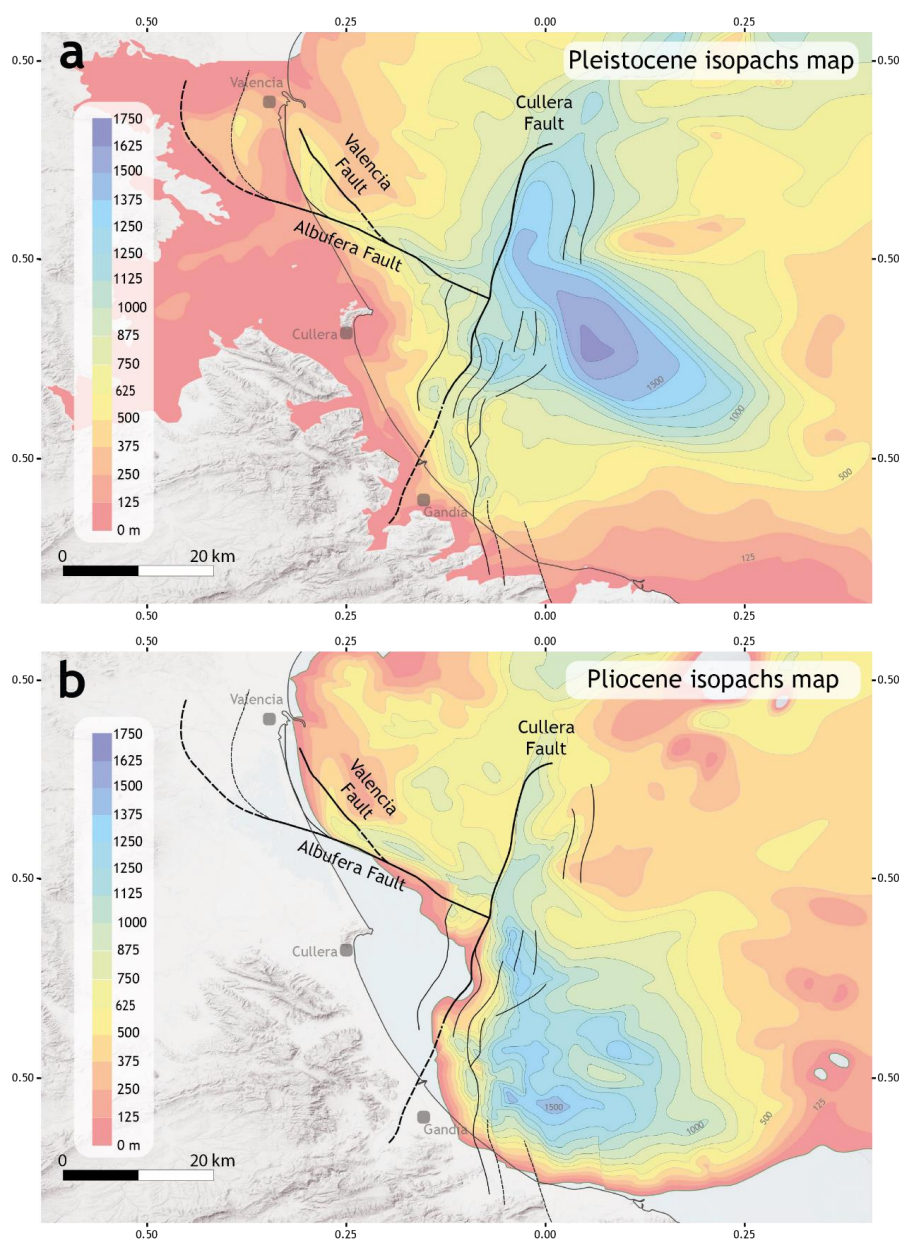


Figure 4: Chronostratigraphic diagram of the southwestern Valencia Trough.

Note that the depth scale shows maximum thicknesses of units.



311

312 Figure 5. Isopach maps of the southwestern Valencia Trough for the Pleistocene (a)

313 and Pliocene (b). The traces of the active faults are also depicted. Fault traces

314 represent the horizontal projection of the direction line of the fault plane, located

315 midway between the intersection line of the top-of-the-Pliocene horizon and the



316 top-of-the-Quaternary horizon. Fault traces are derived primarily from their position
317 on seismic profiles, supplemented by isopach maps and observed thickness
318 variations in stratigraphic units, as indicated by the available wells. Dashed lines
319 show interpreted traces. Modified from Ramos et al. (2025).



320 **5. Main active faults in the southwestern Valencia Trough**

321 In this section, we describe the main structural features of the southwestern
322 Valencia Trough after the analysis of gravity data and isopach maps obtained from
323 the subsurface dataset (seismic lines, wells and VES) (Figs. 3 and 5).

324 The filtered Bouguer anomaly map (Fig. 3) reveals a positive anomaly in the central
325 part of the study area, referred to as the Cullera anomaly. This positive anomaly is
326 surrounded by a region exhibiting a negative anomaly, particularly in the offshore
327 area located east of Cullera. We interpret this pattern of anomaly to be because of
328 mass excess associated with a basement high (Cullera positive anomaly)
329 surrounded by a region with greater sedimentary cover (negative anomaly). This
330 interpretation is further supported by the isopach maps derived from interpretation
331 of the subsurface data (Fig. 5). The negative gravity anomaly correlates with an
332 abrupt increase in the thickness of both the Pliocene and Quaternary sedimentary
333 successions. Furthermore, the transitions in both the gravity anomaly and
334 sedimentary thickness correspond to the positions of the main faults observed in
335 the seismic dataset (see below). On the basis of this evidence, we propose that the
336 southwestern Valencia Trough is structurally characterised by the presence of three
337 major faults offsetting the basement and significantly influencing the stratigraphic
338 evolution of the area. These three major faults are: the Cullera Fault, the Valencia
339 Fault and the Albufera Fault (Fig. 5).

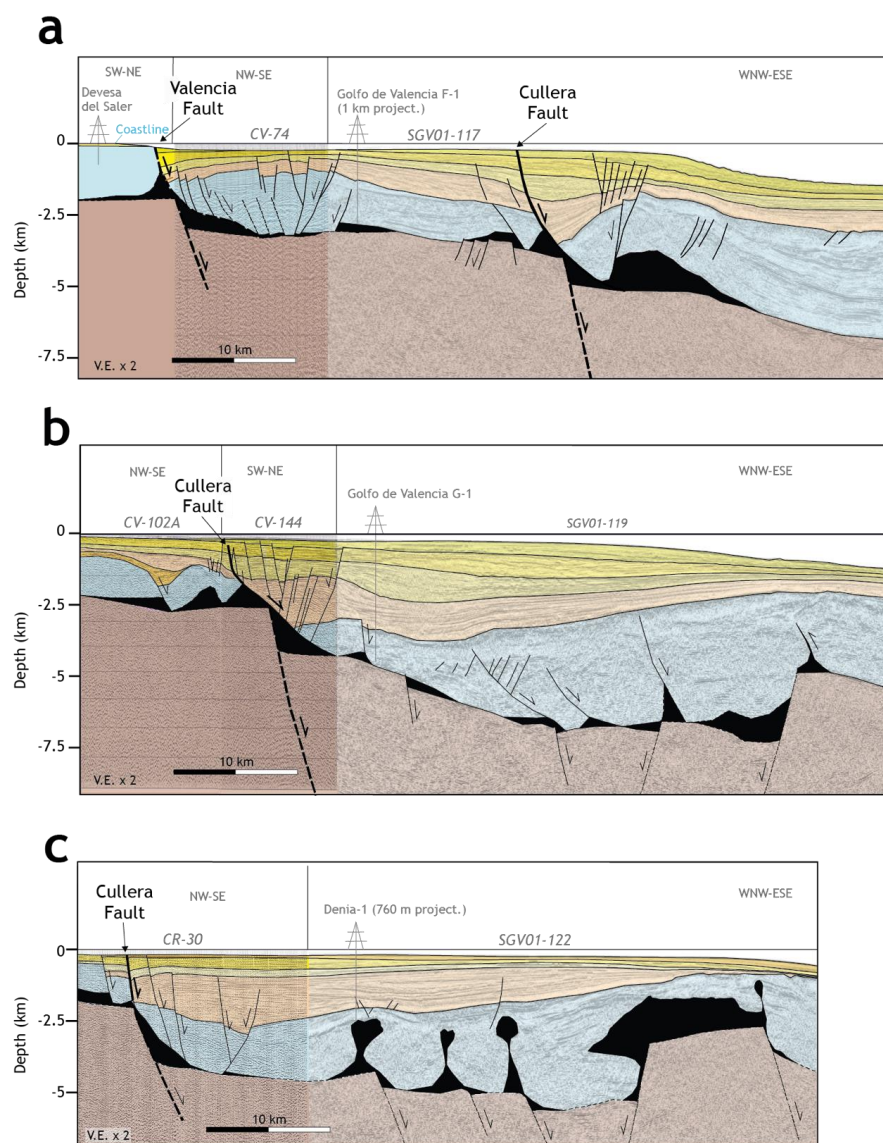
340 The structural configuration of the southwestern Valencia Trough is also influenced
341 by the presence of Upper Triassic evaporites and shales at the base of the Mesozoic
342 sedimentary cover. This mechanically weak layer induces tectonic decoupling
343 within the seismogenic crust of the southwestern Valencia Trough. As a result, the
344 deformation style of the suprasalt succession (cover) differs significantly from that
345 of the subsalt succession (basement) (Etheve et al., 2018; Fang et al., 2021; Ramos
346 et al., 2023, 2025; Roma et al., 2018).

347 The analysis of the seismic reflection profiles (Fig. 6) reveals three distinct fault
348 types: i) faults restricted to the subsalt basement; ii) faults restricted to the

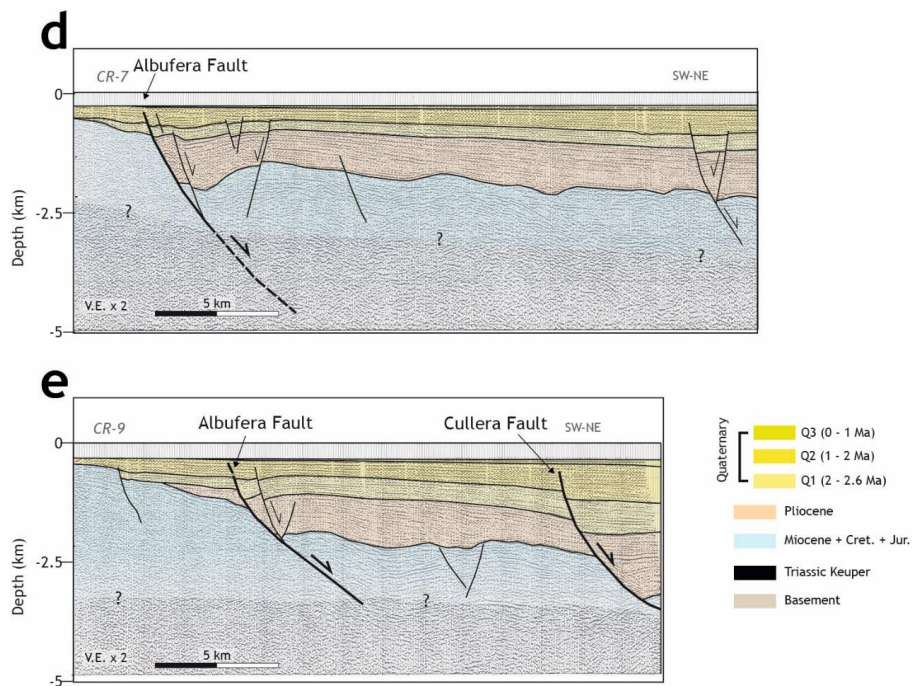


349 suprasalt cover; and iii) faults cutting through the sedimentary cover, basement and
350 salt layer.

351



352



353

354 Fig. 6. Interpreted sections derived from onshore cross-sections (a) and the offshore
355 2D seismic profiles (a-e). See Fig. 3 for the location. a-c sections after Ramos et al.,
356 2025.

357

358 5.1 Cullera Fault

359 The Cullera Fault is the longest along-strike fault in the region, spans approximately
360 59 km, and has the highest cumulative offset, with more than 1800 m of vertical
361 displacement at the top of the Messinian horizon (Figs. 5 and 6).

362 The along-section geometry of the fault across the suprasalt succession is well
363 imaged in the seismic reflection dataset (Fig. 6). The Cullera Fault is a normal, NNE–
364 SSW-trending fault that dips highly towards the east. The fault offsets the entire
365 suprasalt cover, including the 1 Ma horizon. Owing to the low resolution of the
366 available bathymetric data, it is not possible to confirm whether the fault offsets the
367 seafloor. The Cullera Fault displaces the top of the basement horizon, indicating
368 that this fault involves both subsalt and suprasalt successions.

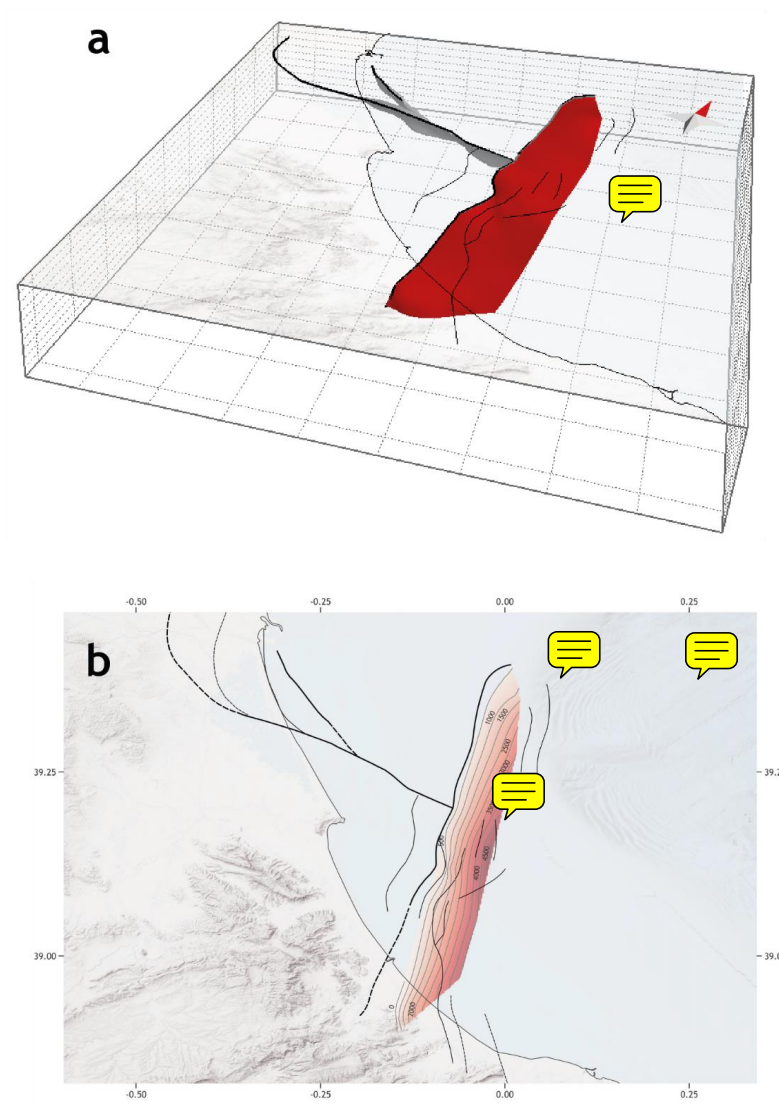


369 Within the basement, the Cullera Fault is poorly imaged in seismic profiles.
370 Nevertheless, the available data suggest that it is a planar fault (Fig. 6). This is also
371 supported by the absence of significant tilting of the basement-top horizon.

372 In contrast, the geometry of the Cullera Fault in the sedimentary cover is
373 heterogeneous. In the northern area (Fig. 6), the part of the Cullera Fault offsetting
374 the cover exhibits a listric geometry, which is responsible for the development of a
375 rollover structure in the hanging wall (Fig. 6). This listric geometry consists of a highly
376 dipping (50–60°) upper part offsetting the Plio-Quaternary succession and a gently
377 dipping (20–30°) lower part in the Mesozoic cover. Southwards, the listric geometry
378 and related rollover fold becomes less pronounced (Fig. 6).

379 To better constrain the geometry of the Cullera Fault, we constructed a structural
380 map of the fault by integrating fault traces identified in the seismic reflection dataset
381 with isopach maps (Fig. 7). Additionally, a 3D model of the Cullera Fault, along with
382 the two other major faults, was generated following a 2½D construction approach,
383 integrating interpreted seismic profiles via interpolation. We employed the ordinary
384 kriging algorithm implemented in MOVE software, a methodology consistent with
385 previous approaches applied to analogous structures (Ramos et al., 2020), ensuring
386 a geologically consistent representation of the fault geometry in the subsurface.
387 This approach allows for the reconstruction of complex fault surfaces by integrating
388 available geophysical data while minimising spatial uncertainties. Analysis of the
389 reconstructed 3D fault indicates that the surface area of the Cullera Fault offsetting
390 the sedimentary cover is approximately 360 km².

391



392

393 Figure 7. 3D model (a) and structural map (b) of the Cullera Fault (red surface).
 394 Squares in figure a represent 10 km x 10 km. Note the red arrow pointing to the North
 395 in figure a.

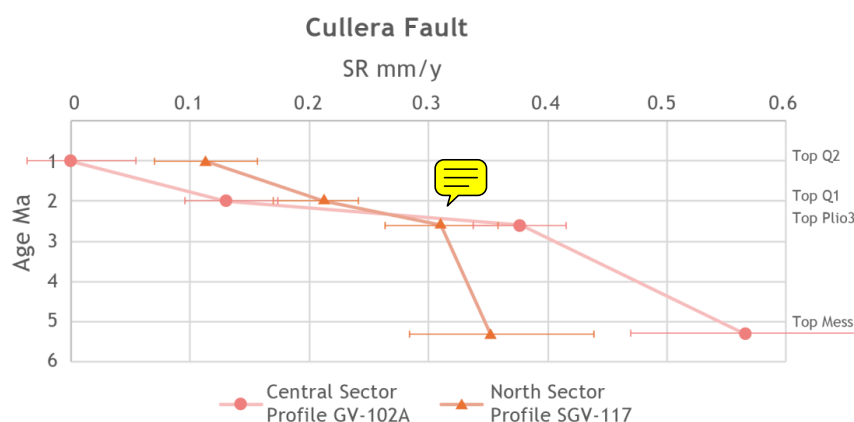
396

397 Several minor normal faults have developed in the hanging wall of the Cullera Fault
 398 (Figs. 5). These faults displace only the suprasalt succession without affecting the



399 underlying subsalt units. In previous studies (e.g., Perea 2006; Roca 1992) distinct
400 names were assigned to these faults, such as the Western Cabo Cullera Fault,
401 Central Cabo Cullera Fault, and Eastern Cabo Cullera Fault. However, the improved
402 resolution and quality of the new seismic dataset enable a more detailed
403 characterisation of these tectonic structures, allowing for a reassessment of their
404 nomenclature and role. On the basis of our analysis, we interpret these minor faults
405 to be part of the damage zone associated with the main Cullera Fault. Fault damage
406 zones typically consist of subsidiary structures that develop in response to the
407 distribution of strain surrounding a major fault. In this context, these minor faults
408 represent secondary features that contribute to the overall deformation but are
409 structurally subordinate to the Cullera Fault. Consequently, we propose
410 consolidating the nomenclature to avoid potential confusion. Instead of assigning
411 separate names to these subsidiary faults, we retain the term Cullera Fault
412 exclusively for the main structure.

413 The quality of the seismic dataset in profiles GV-102A and SGV-117 (Fig. 3) allows for
414 an analysis of the slip rate of the Cullera Fault. This analysis is approximate,
415 because of the resolution of the seismic profiles, the uncertainties in the recognition
416 of the markers in the hanging wall and footwall, and the age of these markers. Net
417 slip rates were obtained for the Top-Messinian, Top Pliocene, Top-Q1, and Top-Q2
418 horizons, with assigned ages of 5.3 Ma, 2.6 Ma, 2 Ma, and 1 Ma, respectively.
419 Analogous values of the slip rate for each of these markers were obtained from the
420 two analysed seismic profiles (Fig. 8). The slip rates for the Cullera Fault seem to
421 have decreased over time, as the calculation yielded mean slip rates of 0.40 ± 0.1
422 mm/y for the Pliocene and 0.15 ± 0.1 mm/y for the Quaternary. However, we cannot
423 dismiss that this apparent in-time evolution could be an artefact related to the
424 epistemic uncertainties mentioned above.



425

426 Figure 8. Long term slip rates (SR) for the Cullera Fault derived from the seismic
 427 profiles for the Top Messinian, Top Plio3, Top Q1, and Top Q2 horizons. Pink line and
 428 dots represent SR for the central sector of the fault. Orange line and triangles
 429 indicate SR for the north sector of the fault. Slip rates seem to decrease in time, from
 430 0.40 ± 0.1 mm/y for the Pliocene to 0.15 ± 0.1 mm/y for the Quaternary. Error bars
 431 are estimated on the basis of uncertainties in the recognition of the markers and
 432 their ages.

433

434 5.2. Albufera Fault


435 The Albufera Fault (F3) (Figs. 5 and 6) is a newly defined active structure in the
 436 southwestern Valencia Trough. This NW–SE striking fault extends approximately 55
 437 km and exhibits a maximum normal offset of 1000 m for the Top-Messinian horizon.
 438 This would imply a long-term slip rate of 0.2 ± 0.1 mm/y. The fault offsets both the
 439 supra- and subsalt successions (Figs. 5 and 6). The Albufera Fault is visible only in
 440 the vintage seismic reflection dataset, where it presents a low dip and a listric
 441 geometry.

442 The Albufera Fault appears to offset the entire suprasalt cover, including the 1 Ma
 443 horizon. As with other faults in the region, the low resolution of the available
 444 bathymetric data prevents us from determining whether this fault offsets the
 445 seabed. Nevertheless, high-resolution seismic profiles from the offshore shelf
 446 analysed by previous authors indicate seabed offsets caused by secondary normal



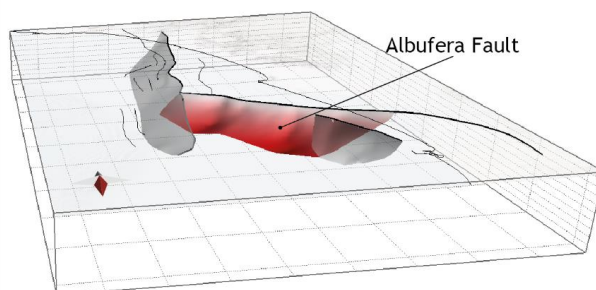
447 faults likely associated with the Albufera Fault (Díaz de Río et al., 1986; Albarracín
448 et al., 2013).

449 The available seismic dataset reveals a normal kinematic component for the
450 Albufera Fault. However, mapping of small-scale fault traces in upper Pleistocene–
451 recent sediments (interval between the seabed and the 1.8 Ma horizon) reveals that
452 these faults are oblique to the main trend of the Albufera Fault, forming an en
453 echelon pattern in map view, which suggests that the Plio-Quaternary reactivation
454 of the main fault has a significant right-lateral strike-slip component. This dextral
455 component along the NW–SE trending fault is consistent with the regional ENE–
456 WSW direction of Plio-Quaternary extension in the southwestern Valencia Trough
457 and kinematically consistent with NNW–SSE trending normal faults. The fault
458 influences the Plio-Quaternary sedimentary infill of the southwestern Valencia
459 Trough (Fig. 5). The computed isopach maps reveal that the Pliocene succession
460 significantly increased in the hanging wall relative to the footwall. Similarly, the
461 Quaternary succession is thicker in the hanging wall than in the footwall. The listric
462 geometry of the Albufera Fault is responsible for the development of a rollover
463 anticline in the hanging wall (Fig. 6). This anticline is likely accentuated by the
464 palaeoshelf edge of the late Tortonian–early Messinian shelf, which is located in the
465 central part of the rollover structure.

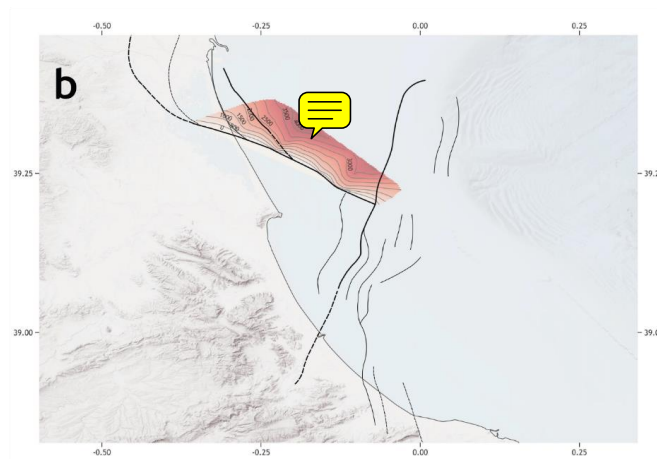
466 To further constrain the geometry of the Albufera Fault, a structural map of the
467 fault was constructed (Fig. 9). Analysis of the reconstructed 3D fault surface
468 indicates that the fault encompasses an area of approximately 560 km². 



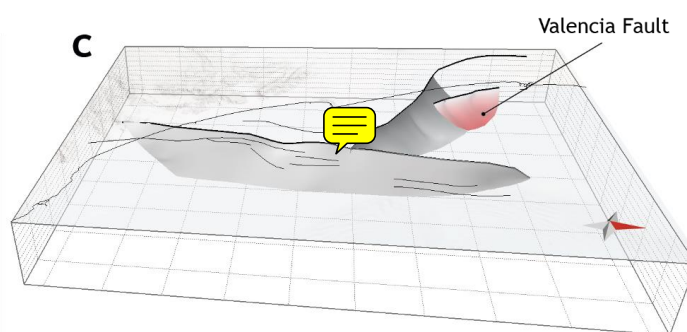
a



b



c



469

470

471

472

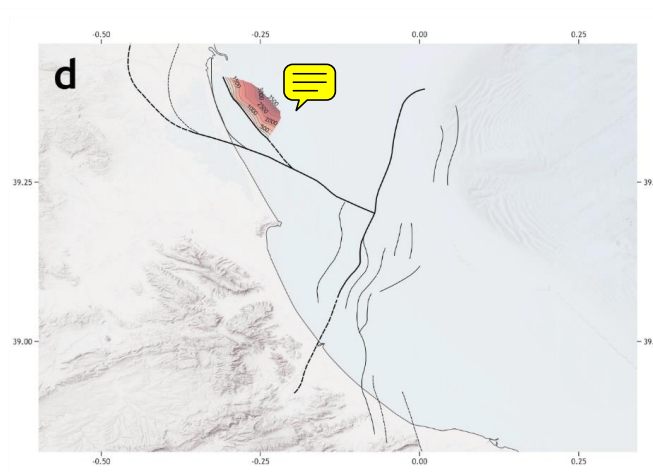
473

474

475

476

477



478

479 Figure 9. 3D model and structural map of the Albufera Fault (a and b) and the
480 Valencia Fault (c and d). Squares in 3D models represent 10 km x 10 km. Note the
481 red arrow pointing to the North in figures a and c.

482

483

484 5.3 Valencia Fault

485 In this section, we define ~~for the first time~~ the Valencia Fault (Figs. 5 and 6). This
486 structure is considered one of the main active faults in the southwestern Valencia
487 Trough because of its length of approximately 20 km and its significant impact on
488 the distribution of Quaternary depocentres. The Valencia Fault displaces both the
489 supra- and subsalt successions (see below) (Figs. 5 and 6).

490 This NNW–SSE trending, steeply dipping fault is imaged primarily in the vintage
491 seismic reflection dataset, where it exhibits a listric geometry, at least in the portion
492 offsetting the suprasalt succession (Fig. 6). The Valencia Fault offsets the entire
493 suprasalt cover, including the 1 Ma horizon. However, owing to the low resolution of
494 the available bathymetric data, it is not possible to determine whether this fault
495 offsets the seabed. The Valencia Fault also displaces the top of the basement
496 horizon, indicating that this structure involves both subsalt and suprasalt
497 successions. Within the basement, the Valencia Fault is not well-imaged in the



498 seismic profiles, but the absence of tilting in the basement-top horizon suggests
499 that it is a planar fault (Fig. 6). The Valencia Fault and its secondary strands very
500 likely continue onshore below the City of Valencia. The lack of onshore seismic data
501 hampers the mapping of these fault strands, but their presence can be inferred from
502 the abrupt Plio-Quaternary thickness changes observed in water wells and Vertical
503 Electric Sounding profiles.

504 To further constrain the geometry of the Valencia Fault, a structural map of the fault
505 was constructed (Fig. 9). Analysis of the reconstructed 3D fault surface indicates
506 that the fault encompasses an area of approximately 208 km².

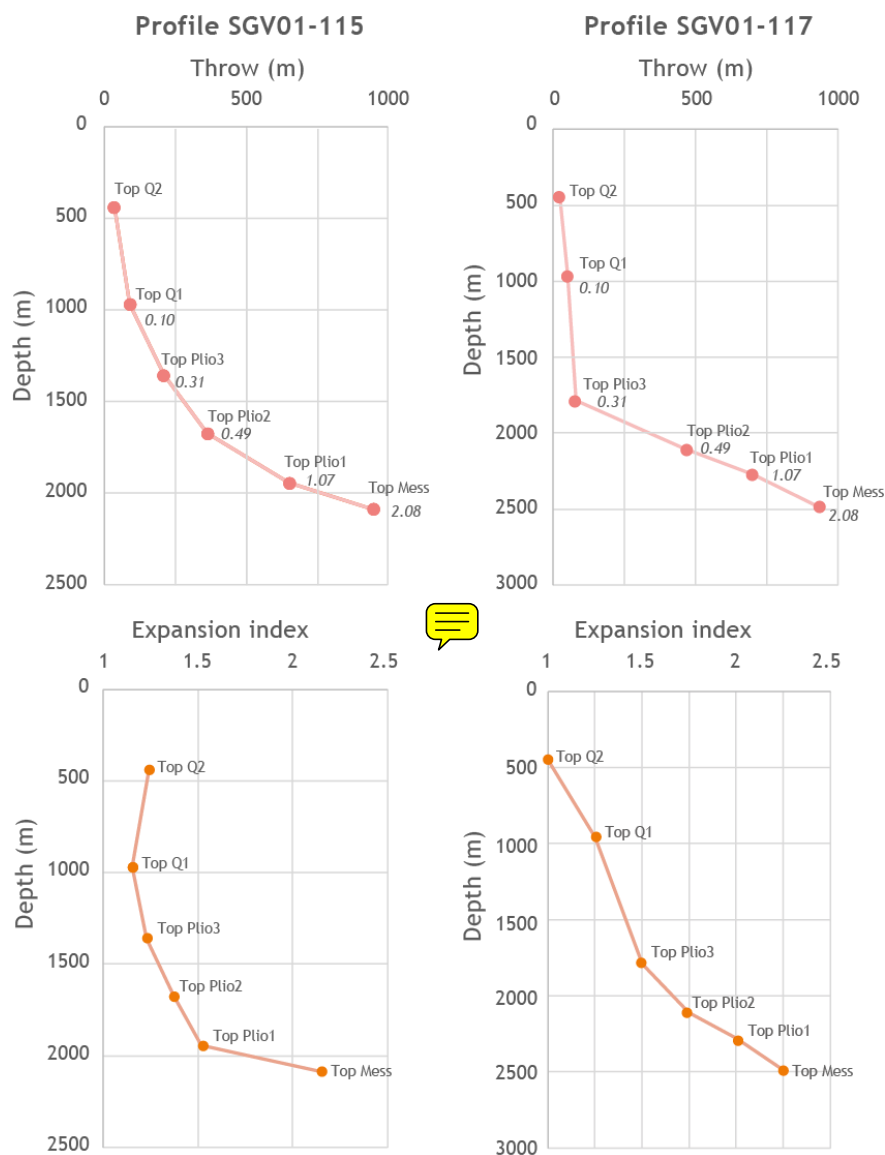
507



508 **6. Evolutionary growth of the Cullera Fault: interplay between tectonics and**
509 **salt withdrawal.**

510 This section aims to provide further insights into the evolution of the active faults in
511 the southwestern Valencia Trough. The low resolution of the vintage seismic dataset
512 limits the ability to perform a detailed analysis only for the Cullera Fault. To analyse
513 recent along-dip variations in throw, we constructed throw-depth plots (T-z plots)
514 for the post-Messinian markers (Fig. 10). These plots provide insights into the
515 evolutionary growth of the fault (Mansfield and Cartwright, 1996; Hongxing and
516 Anderson, 2007). The quality of the available seismic reflection dataset allows this
517 analysis to be performed on two seismic profiles located in the northern part of the
518 fault, where the listric geometry is well-developed (LINES SGV01-115 and SGV01-
519 117; Fig. 6).

520 We computed T-z plots for six suprasalt horizons: Top-Messinian, Top Plio1, Top
521 Plio2, Top Plio3, Top Q1, and Top Q2 (Fig. 10). The T-z plots for the Cullera Fault reveal
522 a general increase in the throw and throw gradient with depth. However, the data
523 indicate two distinct portions with differing throw gradients: (i) the lower portion,
524 with higher throw gradients, includes horizons from the Top Messinian to the Top
525 Pliocene; (ii) the upper portion, with lower throw gradients, comprises the
526 Quaternary horizons. This distinction between these two portions is particularly
527 pronounced in the southern seismic line (line SGV01-117, Fig. 6). Here, the throw
528 gradient decreases, from 2.38-2.98 in the lower portion to 0.22-0.10 in the upper
529 portion.



530

531 Figure 10. Throw depth (T-z) and expansion index plots for the Cullera Fault
 532 computed from profiles SGV01-115 and SGV01-117. The numbers within the T-z
 533 plots indicate the throw gradient for the corresponding interval. The T-z plots reveal
 534 an increase in the throw and throw gradient, with a higher throw gradient for the Top
 535 Messinian–Top Pliocene interval and a lower throw gradient for the Quaternary
 536 interval.



537 The Cullera Fault significantly influences the Plio-Quaternary sedimentary infill of
538 the southwestern Valencia Trough. Isopach maps indicate a marked increase in the
539 thickness of both Pliocene and Quaternary successions in the hanging wall with
540 respect to the footwall (Fig. 5). This thickness variation offers critical insights into
541 the history of fault growth. To quantify this relationship, we computed the expansion
542 index (Thorsen, 1963; Rouby et al., 2003; Jackson and Rotevatn, 2013) for the post-
543 Messinian stratigraphic units (Fig. 10). The expansion index consistently exceeds 1
544 across all the analysed intervals, indicating a synkinematic deposition in these
545 units. Notably, the Pliocene units exhibit a greater expansion index than the
546 Quaternary units do, with the difference being particularly pronounced in the
547 southern seismic line (Fig. 6 LINE SGV01-117).

548 Finally, to shed light on the mechanisms controlling the creation of accommodation
549 space related to the Cullera Fault, we analyse the tectonic–stratigraphic
550 arrangement of the hanging wall units. In the northern part of the Cullera Fault,
551 where the rollover structure is well developed (Fig. 6), the position of the Plio-
552 Quaternary depocenter in the hanging-wall varies along the dipdirection. The
553 Pliocene depocentre remains in the immediate hanging wall of the fault. However,
554 during the deposition of unit Q1, the depocentre migrated basinwards. The
555 depocentre of unit Q2 is located adjacent to the fault, whereas the depocentre of
556 unit Q3 is located further east, related to the progradational geometry of the
557 sedimentary bodies. Nevertheless, when focusing strictly on the area affected by
558 the fault, the local Q3 depocentre also remains adjacent to the fault.

559 Analogous stratigraphic geometries have been observed in the Danish North Sea,
560 where they have been interpreted in terms of the evolution of a salt-influenced fault
561 (Duffy et al., 2023 and references therein). In such a setting, two mechanisms create
562 accommodation space: fault displacement and load-driven salt withdrawal in the
563 hanging-wall. These two mechanisms can act separately or contemporaneously in
564 time. When the accommodation space generated by the fault offset exceeds that
565 created by salt withdrawal, the depocentre axis remains adjacent to the fault. In
566 contrast, when salt-related accommodation space is dominant, the depocentre
567 migrates away from the fault (Duffy et al., 2023).



568 Accordingly, we interpret that, during the Pliocene, the accommodation space
569 generated by the displacement of the Cullera Fault exceeded that produced by the
570 accommodation space related to salt withdrawal, as evidenced by the depocentre's
571 axis being located adjacent to the fault (Fig. 6). During the deposition of unit Q1, the
572 depocentre migrated basinwards, suggesting that salt withdrawal-related
573 accommodation space outpaced that related to fault displacement. Finally, during
574 Q2 and Q3, the depocentre axis shifted towards the fault, indicating that fault
575 displacement-related accommodation space regained dominance over salt
576 mobility.

577 All the above-described features shed light on the evolution of the salt-influenced
578 Cullera Fault. As previously discussed, the creation of accommodation space
579 results from two mechanisms: tectonic offset along the fault and displacement
580 related to salt withdrawal. Both mechanisms act cumulatively; that is, both
581 mechanisms produce slip along the Cullera Fault and create accommodation
582 space. The migration of successive depocentres suggests that, during the Pliocene,
583 accommodation space related to tectonic offset was greater than that created by
584 salt withdrawal. As, the throw gradient is high (≈ 2.4) during this period, we postulate
585 that both mechanisms were active. During the deposition of Q1 (2.6–2 Ma), the
586 position of the depocentre suggests that salt mobility became the dominant
587 mechanism, likely due to a decrease in fault activity, an increase in salt withdrawal,
588 or both. As the throw gradient decreases during this period, we postulate that a
589 decrease in the fault displacement rate could be the reason for the change in the
590 main mechanism. Finally, during the rest of the Quaternary (2 Ma to present), fault
591 displacement-related accommodation space once again exceeded that created by
592 salt withdrawal. The constant throw gradient observed during this period with
593 respect to the previous time interval (2.6–2 Ma) suggests that the change in the main
594 mechanism was due to a reduction in or cessation of salt withdrawal. This
595 interpretation is further supported by the off-fault geometry of the Q2–Q3
596 sedimentary bodies, as no significant change in thickness is observed above the salt
597 withdrawal-related anticlinal crest located east of the Cullera Fault (Fig. 6).
598 Therefore, the evolution of the Cullera Fault during the Pliocene–Quaternary time



599 span was controlled mainly by the tectonic offset, except for the time interval

600 between 2.6 and 2 Ma, when offset was related mainly to salt withdrawal.

601



602 **7. Influence of mechanical layering on the seismic potential: the case of the**
603 **southwestern Valencia Trough**

604 The southwestern Valencia Trough has a distinct mechanical stratigraphy
605 characterised by a subsalt basement and a suprasalt Mesozoic–Quaternary
606 sedimentary succession. These two units are separated by a **weak mechanical layer**
607 composed of Triassic evaporites. **These lithologies** are well documented for their
608 ductile behaviour, which enables them to act as regional detachment layers (e.g.,
609 Morley et al., 2003; Jackson and Hudec, 2005) and inhibits the propagation of faults
610 (e.g., Withjack et al., 1990; Pascoe et al., 1999; Maurin and Nivière, 2000; Withjack
611 and Callaway, 2000; Richardson et al., 2005; Ford et al., 2007; Kane et al., 2010;
612 Marsh et al., 2010). Moreover, mechanically weak layers have been shown to induce
613 full or partial geometric and kinematic decoupling between sub- and
614 supradetachment successions (e.g., Stewart et al., 1997; Withjack and Callaway,
615 2000; Ford et al., 2007; Tvedt et al. 2013). In this section, we focus on the
616 implications of this mechanical arrangement in terms of the seismic potential of
617 salt-influenced active faults.

618 In an active region, tectonics are generally the main driving mechanism of fault
619 displacement. However, in the case of salt-influenced faults, displacement can
620 also result from salt withdrawal. Our analysis of the evolution of the Cullera Fault
621 presented in the previous section indicates that the fault offset is related to the
622 interplay between two mechanisms: tectonic offset along the fault and
623 displacement related to salt withdrawal. Our analysis also reveals how these two
624 processes interact with each other. Consequently, in areas with salt-influenced
625 faults, seismicity can potentially be produced from either mechanism or a
626 combination of both.

627 In terms of seismic potential, there is a significant difference between a tectonic
628 earthquake and a salt-withdrawal earthquake. This difference lies in the maximum
629 potential thickness of the seismogenic layer involved in the rupture. A tectonically
630 driven earthquake could theoretically rupture the entire seismogenic crust. **In**
631 **contrast, a salt withdrawal-related earthquake would imply offset restricted to the**
632 **suprasalt succession.** Therefore, in an earthquake restricted to the suprasalt



633 succession, the thickness of the seismogenic layer is limited by the depth of the
634 mechanically weak layer, reducing the maximum potential rupture area and,
635 consequently, the seismic potential. A salt-withdrawal-related earthquake could
636 induce a vertical stress drop related to salt displacement, potentially triggering
637 displacement in the subsalt succession and leading to a complex rupture. However,
638 in terms of seismic potential, such a hypothetical earthquake would not differ from
639 a tectonically-driven event. Similarly, a tectonically driven earthquake may rupture
640 only the suprasalt succession.

641 Despite the mechanism driving seismicity the presence of a weak mechanical layer
642 within the seismogenic crust significantly influences the seismogenic potential of
643 active faults. We hypothesise that this weak layer could locally hinder the effective
644 vertical propagation of a rupture, thereby resulting in faults being seismogenically
645 bonded. Specifically, the total or partial decoupling induced by the weak evaporitic
646 layer may limit the effective width of the seismogenic layer. This hypothesis is
647 independent of the weak layer composition; therefore, our hypothesis can be
648 extended to any region with a similar structural configuration.

649 A widely used approach to characterise the seismic potential of an active fault
650 involves earthquake fault scaling relationships. These relationships estimate the
651 seismic parameters of an active fault on the basis of its geometric and/or kinematic
652 features (Kanamori and Anderson, 1975; Geller, 1976; Wells and Coppersmith;
653 1994; Stirling et al., 2002 and 2013; Leonard, 2010 and 2014; among many others).
654 In the case of the southwestern Valencia Trough faults, the available data support
655 characterisation on the basis of geometric features, such as fault area, length, or
656 width. However, the mechanical layering observed in the southwestern Valencia
657 Trough necessitates the cautious application of these scaling relationships. The
658 influence of the weak mechanical layer introduces complexities that may not be
659 fully accounted for by traditional scaling methods.

660 Therefore, we begin our analysis by comparing the southwestern Valencia Trough
661 with the Zagros fold-and-thrust belt. While Zagros fold-and-thrust belt differs
662 tectonically from the southwestern Valencia Trough, as it is dominated by
663 shortening rather than extension, it structurally resembles the southwestern



664 Valencia Trough because of its pronounced mechanical layering in the upper crust.
665 The Zagros fold-and-thrust belt features a crystalline basement overlain by a 10-km-
666 thick Precambrian–Quaternary sedimentary cover. These two successions are
667 separated by the Hormuz salt layer (Casciello *et al.*, 2009; Sherkati *et al.*, 2005;
668 Molinaro *et al.*, 2005). That is, similar to the southwestern Valencia Trough, the
669 seismogenic crust is characterised by the presence of an intermediate
670 mechanically weak layer. Seismicity in the Zagros fold-and-thrust belt is
671 characterised by a general absence of coseismic surface ruptures. This seismicity
672 nucleates both in the basement and in the cover (Nissen *et al.*, 2011). Notably, the
673 centroids of most of the larger events (magnitudes exceeding M_w 5), are located at
674 depths between 4 and 14 km, indicating that seismic activity nucleates both within
675 the suprasalt succession and in the basement (Nissen *et al.* 2007, 2010; Roustaei
676 *et al.* 2010). Additionally, very large earthquakes have occurred in the Zagros fold-
677 and-thrust belt; these earthquakes include the Ghir and Khurgu events ($M_w=6.7$),
678 which are interpreted as ruptures involving both the basement and the cover,
679 rupturing through the basement–cover interface (Nissen *et al.*, 2011).

680 We propose that the southwestern Valencia Trough may exhibit a comparable
681 pattern of seismicity to that of the Zagros fold-and-thrust belt. Specifically, we
682 hypothesise that seismic events in the southwestern Valencia Trough could have
683 nucleated within both the basement and the suprasalt succession. Furthermore, we
684 postulate that larger earthquakes in the southwestern Valencia Trough could also
685 rupture both mechanical layers. Available centroid data for the southwestern
686 Valencia Trough suggest that most earthquakes nucleate at depths between 1 and
687 13 km (Fig. 2). Although these depth estimates carry significant uncertainties, we
688 interpret this dataset as supporting evidence for our hypothesis that seismicity in
689 the southwestern Valencia Trough nucleates both in the basement and in the cover.

690 As we mentioned previously, most empirical source-scaling relationships for crustal
691 earthquakes correlate the moment magnitude (M_w) with the fault dimensions
692 (length, width, and/or area; (Kanamori and Anderson, 1975; Geller, 1976; Wells and
693 Coppersmith; 1994; Stirling *et al.*, 2022; Leonard, 2010; among many others). We
694 propose that when these scaling relationships are applied to regions with a weak



695 mechanical layer, the role of this layer should be explicitly considered in the
696 analysis. This is because the presence of a weak layer can potentially hinder the
697 effective vertical propagation of a rupture, thereby limiting the effective width of the
698 seismogenic layer. This consideration is particularly relevant for earthquakes that
699 nucleate above the weak layer.

700 Several studies suggest that the downdip width of the seismogenic crust (the
701 thickness of seismogenic crust measured along the fault plane) can constrain the
702 maximum magnitudes of earthquakes (Hyndman, 2007; Ruff and Kanamori, 1983;
703 Weng & Yang, 2017). For large-magnitude events involving the entire seismogenic
704 crust, some scaling relationships account for the constraint on fault-width rupture
705 growth relative to fault-length rupture growth by incorporating a change in slope in
706 width-to-length scaling (Leonard, 2010; Yen and Ma, 2011; Leonard, 2014; Cheng et
707 al., 2019; Huang et al., 2024). This change in slope reflects the width of the
708 seismogenic crust, which imposes a limit on rupture propagation owing to
709 variations in the mechanical behaviour of the crust. We propose a similar approach
710 to evaluate the seismic potential of regions characterised by a weak mechanical
711 layer within the upper crust, such as the southwestern Valencia Trough.

712 Our approach involves including the rupture aspect ratio when calculating the
713 geometric parameters of an active fault. Specifically, we propose that, instead of
714 using the total area or length of the fault as direct inputs to scaling relationships, a
715 correction factor should be applied to these geometric parameters. This correction
716 factor is based on the empirical aspect ratio of faults. For example, consider an
717 earthquake nucleating above a weak mechanical layer. Two potential scenarios for
718 the propagation of such an earthquake can be envisioned: i) that it propagates
719 through the basement–cover interface or ii) that it remains restricted to the
720 succession above the weak layer. In the first scenario, the potential maximum
721 rupture area can be calculated by multiplying the fault length by the fault width. Any
722 area-based or length-based scaling relationship can then be applied. This scenario
723 represents the maximum seismic potential of the fault.

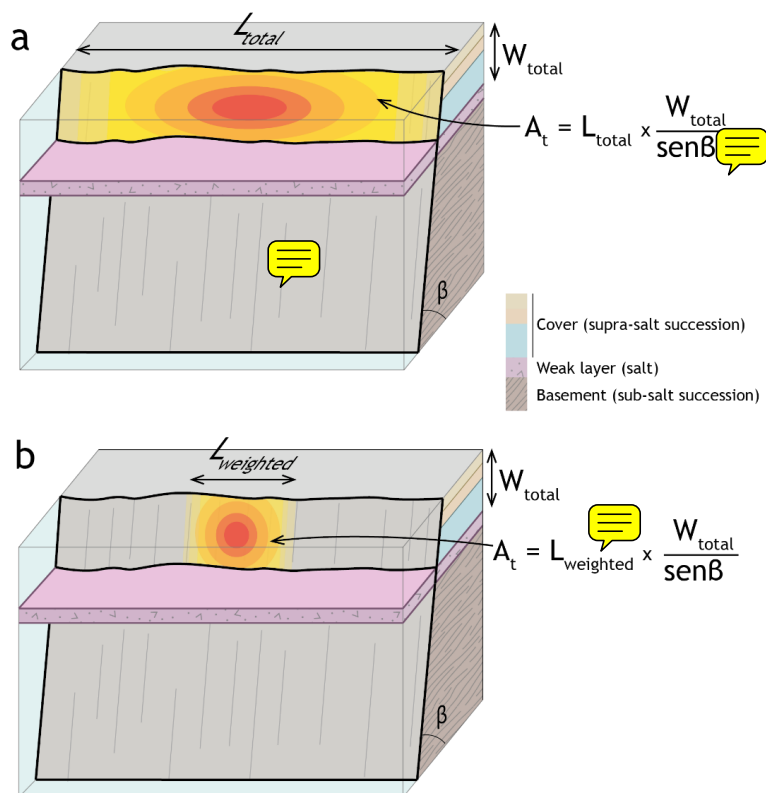
724 In the second scenario, where rupture propagation is restricted to succession above
725 the weak layer, a simplistic calculation of the fault area would multiply the total fault





length by the thickness of the ruptured succession (Fig 11). However, since the
hypothesised rupture offsets only the succession above the mechanically weak
layer, the width of the rupture is significantly limited. This would result in a highly
elongated rupture with an unusually high aspect ratio, deviating from commonly
observed values (Nicol et al., 1996; Stock & Smith, 2000). For this second scenario,
we propose using the thickness of the ruptured succession as a limiting factor.
Specifically, the rupture area should be calculated by multiplying the width of the
fault offset (based on the thickness of the succession above the weak layer and
corrected by the fault dip) by the total fault length weighted by the aspect ratio (Fig
11). This weighted area can then be used as input in any area-based scaling
relationship. We consider that this calculation offers a more realistic estimation of
the maximum seismogenic potential for events rupturing only the succession above
the weak layer. Finally, we recommend avoiding length-based scaling relations for
this second scenario, as such relations implicitly assume a rupture of the entire
seismogenic crust.





741

742 Figure 11. Conceptual model of the weighted rupture area of an earthquake
 743 nucleating above the weak mechanical layer. The area of the rupture is
 744 shown using a red–yellow gradient. An earthquake rupturing the total fault
 745 length (L) and the total thickness (W_{total}) above the weak layer would result in
 746 nonrealistic, highly elongated ruptures. In figure panel b, we propose a more
 747 realistic case: an earthquake offsetting the total thickness above the weak
 748 layer (W_{total}) and a rupture length weighted by the aspect ratio (L_w).

749

750



751 **8. Seismic characterisation of active faults in the southwestern Valencia**
752 **Trough.**

753 In this section, we compute the seismic potential of the active faults in the
754 southwestern Valencia Trough by applying several scaling relationships. We perform
755 two distinct calculations corresponding to the two scenarios described earlier. i) In
756 the first scenario, we assume a rupture involving both the supra- and subsalt
757 successions. That is, this first scenario accounts for an earthquake rupturing the
758 entire seismogenic crust. This scenario provides the maximum seismic potential of
759 the faults. ii) In the second scenario, we assume that a rupture is restricted to the
760 suprasalt succession. For this calculation, we apply several area-based scaling
761 relationships, and we use the area weighted by the aspect ratio as the input
762 parameter. Since the rupture area involved in this second scenario is relatively
763 small, a relatively low seismogenic potential is expected.

764

765 *8.1. First scenario: Ruptures involving the entire seismogenic crust.*

766 For both scenarios, we apply the scaling relationships of Wells & Coppersmith
767 (1994) (values corresponding to normal faults) and Stirling et al. (2002). In the first
768 scenario, i.e., ruptures involving the entire seismogenic crust, we assume that a
769 complete fault ruptured from the subsalt basement through the suprasalt
770 succession. Since the total thickness of the seismogenic crust is not precisely
771 known, we used the fault length as the primary input parameter for these
772 calculations (Table 1).

773

774

775 Table 1 Source parameters obtained from scaling relationships (Wells &
776 Coppersmith, 1994 -WC94- and Stirling et al., 2002 -Stirling02-) assuming ruptures
777 involving the entire seismogenic crust



	Input parameters	WC94			Stirling02	
	L km	M _w	AD m	MD m	M _w	AD m
Cullera Fault	59	7.2 ±0.34	1.61 ±0.37	4.94 ±0.41	7.3 ±0.30	2.39 ±0.24
Albufera Fault	20	6.58 ±0.34	0.42 ±0.37	0.97 ±0.41	6.92 ±0.30	1.97 ±0.24
Valencia Fault	40	6.97 ±0.34	0.99 ±0.37	2.75 ±0.41	7.16 ±0.30	2.23 ±0.24

778

779 8.2. Second scenario: Ruptures involving only the suprasalt succession

780 In this scenario, the presence of a mechanically weak layer within the seismogenic
781 crust is considered to control the seismic potential of active faults. As discussed
782 previously, we use the weighted rupture area as the input parameter for the scaling
783 relationships. The weighting factor is based on the aspect ratio of normal faults. To
784 provide context for this approach, we also present seismic parameters calculated
785 from the total fault area offsetting the entire suprasalt succession. The aspect ratios
786 of normal fault ruptures vary widely (0.4–18); however, most of the observed
787 ruptures are within the range of 0.5 to 3.5 (Nicol et al., 1996; Stock & Smith, 2000),
788 with a mode value of 1.8 (30%, Stock & Smith, 2000). Numerical simulations of
789 strike-slip faults by Weng & Yang (2016) demonstrated that the width of the
790 seismogenic layer significantly influences the rupture aspect ratios. According to
791 their findings, a seismogenic layer thickness of approximately 10 km marks a critical
792 boundary: for thicknesses less than this value, rupture aspect ratios remain low (ca.
793 2), whereas thicknesses greater than 10 km result in significantly higher aspect
794 ratios (<8). Considering these findings and given that the suprasalt succession in the
795 southwestern Valencia Trough has an average thickness of approximately 5 km, we
796 adopt an aspect ratio of 1.8 for our calculations.



797 In the southwestern Valencia Trough, the suprasalt succession thickness (~5 km)
798 and an average fault dip of ~45° yield a maximum rupture width of approximately 7.1
799 km for events confined to the suprasalt succession. For events unrestricted by the
800 aspect ratio (i.e., earthquakes rupturing the entire fault length and width of the
801 suprasalt succession), we compute the rupture area as the product of length and
802 width (L*W). However, when the seismic potential for ruptures weighted by the
803 aspect ratio is calculated, the controlling factor is the fault width. As we assume a
804 constant thickness for the suprasalt succession across southwestern Valencia
805 Trough, the rupture area and corresponding seismic potential are consistent for all
806 the faults in this study (Table 2).

807

808 Table 2 Moment magnitude obtained from scaling relationships (Wells &
809 Coppersmith, 1994 -WC94- and Stirling et al., 2002 -Stirling02-). The first column
810 (not weighted area) corresponds to the values obtained assuming ruptures involving
811 the total suprasalt succession. The second column (weighted area) shows the
812 values obtained using the area weighted by the aspect ratio as input parameter.

	Not weighted area			Weighted area		
	Input parameters A km ²	M _w WC94	M _w Stirling02	Input parameters A km ²	M _w WC94	M _w Stirling02
Cullera Fault	511.4	6.69 ±0.34	7.07 ±0.26	135.2	6.10 ±0.34	6.65 ±0.26
Albufera Fault	346.7	6.21 ±0.34	6.72 ±0.26	135.2	6.10 ±0.34	6.65 ±0.26
Valencia Fault	173.4	6.52 ±0.34	6.94 ±0.26	135.2	6.10 ±0.34	6.65 ±0.26

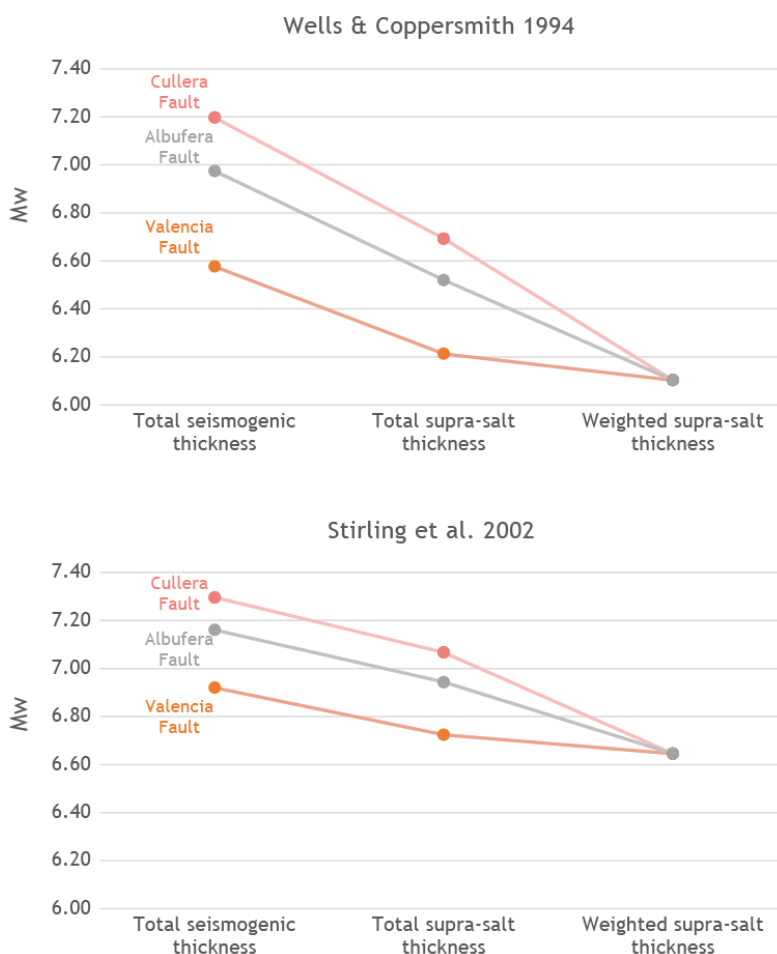
813



814 The comparison between the standard application of earthquake source scaling
815 relations and the approach presented here for regions characterised by the
816 presence of a weak mechanical layer within the seismogenic crust reveals
817 significant differences (Fig. 12). The maximum expected magnitudes for
818 characteristic events rupturing the entire seismogenic crust (i.e., propagating
819 across the basement–cover interface) are estimated to be 7.2–7.3, 6.58–6.92, and
820 6.97–7.16 for the Cullera, Valencia, and Albufera Faults, respectively. In contrast, for
821 hypothetical earthquakes restricted to the suprasalt succession and rupturing of
822 the total length of the faults, the expected magnitudes are lower, ranging from 6.7–
823 7.1, 6.2–6.7, and 6.5–6.9 for the Cullera, Valencia, and Albufera faults, respectively.
824 However, in such cases, we argue that the seismic potential derived using area-
825 weighted relations provides a more realistic estimate. Using this approach, our
826 calculations yield maximum magnitudes of 6.1–6.7 for all faults. These values are
827 2–9 % lower than those obtained when accounting for the total suprasalt
828 succession thickness.

829 When the area-weighted values are compared with the maximum expected
830 magnitudes for ruptures involving the entire seismogenic crust, the results reveal a
831 4–15% reduction. This discrepancy highlights the importance of incorporating
832 mechanical layering into seismic potential assessments in regions where weak
833 layers influence fault dynamics and rupture propagation. Furthermore, these
834 differences in seismic potential should be addressed in probabilistic seismic hazard
835 assessments.





836

837 Figure 12. Plots of M_w values for the Cullera, Albufera and Valencia Faults obtained
 838 using the scaling relationships of Wells & Coppersmith (1994) and Stirling et al.
 839 (2002). The plots show the values computed assuming a rupture of the total
 840 seismogenic thickness, a rupture of the total suprasalt succession, and the values
 841 assuming a rupture of an area calculated using a suprasalt thickness weighted with
 842 the aspect ratio.

843



844 **9. Conclusions.**

845 Analysis of a comprehensive subsurface dataset from the southwestern Valencia
846 Trough enables the identification of three major active normal faults: the Cullera,
847 Albufera and Valencia faults. Among these faults, the Cullera Fault is the main active
848 structure in this region, with a cumulative offset of 1800 m at the top of the
849 Messinian marker. The long-term slip rate varies over time between 0.15 ± 0.1 mm/y
850 and 0.4 ± 0.1 mm/y. The Albufera Fault, which is 55 km in length, has a long-term slip
851 rate of 0.2 ± 0.1 mm/y, whereas the 20-km-long Valencia Fault significantly
852 influences the spatial distribution of Quaternary depocentres.

853 Our results also reveal heterogeneous seismogenic crust in the study area, largely
854 because of a mechanically weak layer, which is composed mainly of Triassic
855 evaporites. Consequently, two competing mechanisms are responsible for the
856 offset along the active faults: tectonics and salt withdrawal. A quantitative
857 evolutionary analysis of the Cullera Fault indicates that tectonics was the dominant
858 mechanism during the Pliocene, whereas salt withdrawal took precedence in the
859 early Quaternary (2.6–2 Ma). After 2 Ma, tectonic activity once again became the
860 primary driver of fault displacement.

861 The mechanically layered crust of the southwestern Valencia Trough influences
862 seismicity: events may nucleate in either the basement or the suprasalt succession.
863 Total or partial decoupling related to the mechanically weak layer implies that an
864 earthquake that nucleated in the suprasalt succession would likely be restricted to
865 this upper part of the seismogenic crust, yet larger events involving basement and
866 cover units are also plausible. For reliable seismic hazard assessments, both
867 scenarios must be accounted for. To compute the seismogenic potential of active
868 faults under the assumption of rupture within the suprasalt succession, we propose
869 the use of the rupture aspect ratio as a correction factor for the maximum rupture
870 area. Specifically, the product of the suprasalt thickness (corrected by the fault dip)
871 and the fault length—weighted by the aspect ratio—provides a more realistic
872 approximation of the maximum rupture area. Using this method, the maximum
873 magnitudes for suprasalt ruptures are 2–9% lower than those obtained by



874 considering the full suprasalt thickness alone, and 4–15% lower than estimates
875 involving the entire seismogenic crust.

876 Overall, these findings greatly enhance our understanding of the seismogenic
877 potential of the southwestern Valencia Trough, an offshore area near densely
878 populated areas. These findings provide a basis for improved seismic hazard
879 assessments. Additionally, as we are addressing offshore faults exhibiting vertical
880 displacement, our findings can be used to establish the tsunamigenic potential of
881 this region. Furthermore, this approach for incorporating mechanical
882 heterogeneities in the seismogenic crust can be applied to other regions and
883 tectonic settings with analogous structural configurations.

884

885



886 **10. Author contribution**

887 Martin-Rojas, I.: Conceptualization, Data curation, Formal analysis, Funding
888 acquisition, Investigation, Methodology, Project administration, Supervision,
889 Validation, Visualization, Writing – original draft preparation, review & editing

890 Ramos, A.: Data curation, Formal analysis, Funding acquisition, Investigation,
891 Resources, Visualization, Writing – original draft preparation, review & editing

892 De Ruig, M.: Data curation, Formal analysis, Investigation, Resources,
893 Visualization, Writing – original draft preparation, review & editing

894 Medina-Cascales, I.: Data curation, Formal analysis, Investigation, Visualization,
895 Writing –review & editing

896 Santamaría-Pérez, E.: Data curation, Formal analysis, Investigation, Writing –
897 review & editing

898 Alfaro, P.: Data curation, Formal analysis, Investigation, Supervision, Writing –
899 review & editing

900

901 **11. Competing interests**

902 The authors declare that they have no conflict of interest.

903

904 **13. Financial support**

905 This research was funded by the Spanish Ministry of Science, Innovation and
906 University (research projects PID2021-127967NB-I00 and RTI2018-100737-B-I00),
907 Generalitat Valenciana (Valencian Regional Government, research projects
908 AICO2021/196 and CIAPOS/2022/082, and University of Alicante (research project
909 VIGROB053). The authors acknowledge the use of the MOVE Software Suite granted
910 by PE Limited (Petex).

911



912

References

- 913 Agustí, J., Santos-Cubedo, A., Furió, M., De Marfá, R., Blain, H., Oms, O., & Sevilla, P.
914 (2011). The late Neogene-early Quaternary small vertebrate succession from the
915 Almenara-Casablanca karst complex (Castellón, Eastern Spain): Chronologic and
916 paleoclimatic context. *Quaternary International*, 243(1), 183–191.
917 10.1016/j.quaint.2010.11.016
- 918 Albarracín, S., Alcántara-Carrió, J., Barranco, A., Sánchez García, M. J., Fontán Bouzas, Á,
919 & Rey Salgado, J. (2013). Seismic evidence for the preservation of several stacked
920 Pleistocene coastal barrier/lagoon systems on the Gulf of Valencia continental shelf
921 (western Mediterranean). *Geo-Marine Letters*, 33(2-3), 217–223. 10.1007/s00367-
922 012-0315-x
- 923 Arche, A., & López-Gómez, J. (1996). Origin of the Permian-Triassic Iberian Basin, central-
924 eastern Spain. *Tectonophysics*, 266(1), 443–464. 10.1016/S0040-1951(96)00202-8
- 925 Bufo, E., & Udías, A. (2021). *El terremoto de Alcoy de 1620 y la serie sísmica de 1644 en*
926 *la comarca de Muro*. Centro Nacional de Información Geográfica.
- 927 Bufo, E., Udías, A., Sanz de Galdeano, C., & Cesca, S. (2015). The 1748 Montesa
928 (southeast Spain) earthquake — A singular event. *Tectonophysics*, 664, 139–153.
929 10.1016/j.tecto.2015.09.005
- 930 Cameselle, A. L., Urgeles, R., De Mol, B., Camerlenghi, A., & Canning, J. C. (2014). Late
931 Miocene sedimentary architecture of the Ebro Continental Margin (Western
932 Mediterranean): implications to the Messinian Salinity Crisis. *International Journal of*
933 *Earth Sciences : Geologische Rundschau*, 103(2), 423–440. 10.1007/s00531-013-
934 0966-5



- 935 Casciello, E., Vergés, J., Saura, E., Casini, G., Fernández, N., Blanc, E., Homke, S., & Hunt,
936 D. W. (2009). Fold patterns and multilayer rheology of the Lurestan Province, Zagros
937 simply folded belt (Iran). *Journal of the Geological Society*, 166(5), 947–959.
938 10.1144/0016-76492008-138
- 939 Cheng Jia, C. J., Rong, Y., Magistrale, H., Chen Guihua, C. G., & Xu Xiwei, X. X. (2019a).
940 Earthquake rupture scaling relations for mainland China. *Seismological Research*
941 *Letters*, 91(1), 248–261. 10.1785/0220190129
- 942 Cheng Jia, C. J., Rong, Y., Magistrale, H., Chen Guihua, C. G., & Xu Xiwei, X. X. (2019b).
943 Earthquake rupture scaling relations for mainland China. *Seismological Research*
944 *Letters*, 91(1), 248–261. 10.1785/0220190129
- 945 Clavell, E., & Berastegui, X. (1991). Petroleum geology of the Gulf of Valencia. *Generation,*
946 *Accumulation, and Production of Europe's Hydrocarbons*, , 355–368.
947 [https://www.scopus.com/inward/record.uri?eid=2-s2.0-](https://www.scopus.com/inward/record.uri?eid=2-s2.0-0026310072&partnerID=40&md5=8f34c3d495738519a9101eb775a91bd4)
948 [0026310072&partnerID=40&md5=8f34c3d495738519a9101eb775a91bd4](https://www.scopus.com/inward/record.uri?eid=2-s2.0-0026310072&partnerID=40&md5=8f34c3d495738519a9101eb775a91bd4)
- 949 De Ruig, & M.J. (1992). *Tectono-sedimentary evolution of the Prebetic fold belt of Alicante*
- 950 Del Rio, V. D., Rey, J., & Vegas, R. (1986). The Gulf of Valencia continental shelf:
951 Extensional tectonics in Neogene and Quaternary sediments. *Marine Geology*, 73(1),
952 169–179. 10.1016/0025-3227(86)90117-9
- 953 DeMets, C., Gordon, R. G., Argus, D. F., & Stein, S. (1994). Effect of recent revisions to the
954 geomagnetic reversal time scale on estimates of current plate motions. *Geophysical*
955 *Research Letters*, 21(20), 2191–2194. 10.1029/94GL02118



- 956 Duffy, O. B., Gawthorpe, R. L., & Docherty, M. (2023). Tectono-stratigraphic evolution of
957 salt-influenced normal fault systems: an example from the Coffee-Soil Fault, Danish
958 North Sea. *Journal of the Geological Society*, 180(6), 1. 10.1144/jgs2023-016
- 959 Etheve, N., Frizon de Lamotte, D., Mohn, G., Martos, R., Roca, E., & Blanpied, C. (2016).
960 Extensional vs contractional Cenozoic deformation in Ibiza (Balearic Promontory,
961 Spain): Integration in the West Mediterranean back-arc setting. *Tectonophysics*, 682,
962 35–55. 10.1016/j.tecto.2016.05.037
- 963 Faccenna, C., Piromallo, C., Crespo-Blanc, A., Jolivet, L., & Rossetti, F. (2004a). Lateral
964 slab deformation and the origin of the western Mediterranean arcs. *Tectonics*
965 (*Washington, D.C.*), 23(1), np–n/a. 10.1029/2002TC001488
- 966 Faccenna, C., Piromallo, C., Crespo-Blanc, A., Jolivet, L., & Rossetti, F. (2004b). Lateral
967 slab deformation and the origin of the western Mediterranean arcs. *Tectonics*
968 (*Washington, D.C.*), 23(1), np–n/a. 10.1029/2002TC001488
- 969 Fang, P., Tugend, J., Mohn, G., Kuszniir, N., & Ding, W. (2021a). Evidence for rapid large-
970 amplitude vertical motions in the Valencia Trough (Western Mediterranean)
971 generated by 3D subduction slab roll-back. *Earth and Planetary Science Letters*, 575,
972 117179. 10.1016/j.epsl.2021.117179
- 973 Fang, P., Tugend, J., Mohn, G., Kuszniir, N., & Ding, W. (2021b). Evidence for rapid large-
974 amplitude vertical motions in the Valencia Trough (Western Mediterranean)
975 generated by 3D subduction slab roll-back. *Earth and Planetary Science Letters*, 575,
976 117179. 10.1016/j.epsl.2021.117179
- 977 Ford, M., Le Carlier de Veslud, C., & Bourgeois, O. (2007). Kinematic and geometric
978 analysis of fault-related folds in a rift setting: The Dannemarie basin, Upper Rhine



- 979 Graben, France. *Journal of Structural Geology*, 29(11), 1811–1830.
- 980 10.1016/j.jsg.2007.08.001
- 981 García-Mayordomo, J., Insua-Arévalo, J. M., Martínez-Díaz, J. J., Jiménez-Díaz, A., Martín-
- 982 Banda, R., Martín-Alfageme, S., Álvarez-Gómez, J. A., Rodríguez-Peces, M., Pérez-
- 983 López, R., Rodríguez-Pascua, M. A., Masana, E., Perea, H., Martín-González, F.,
- 984 Giner-Robles, J., Nemser, E. S., & Cabral, J. (2012). The Quaternary active faults
- 985 database of Iberia (QAFI v. 2.0). *Journal of Iberian Geology*,
- 986 38(1)10.5209/rev_JIGE.2012.v38.n1.39219
- 987 Gaspar-Escribano, J. M., Garcia-Castellanos, D., Roca, E., & Cloetingh, S. (2004).
- 988 Cenozoic vertical motions of the Catalan Coastal Ranges (NE Spain): The role of
- 989 tectonics, isostasy, and surface transport. *Tectonics (Washington, D.C.)*, 23(1), np–
- 990 n/a. 10.1029/2003TC001511
- 991 Geel, T. (1995). Oligocene to early Miocene tectono-sedimentary history of the Alicante
- 992 region (SE Spain): implications for Western Mediterranean evolution. *Basin Research*,
- 993 7(4), 313–336. 10.1111/j.1365-2117.1995.tb00120.x
- 994 Geller, R. J. (1976). Scaling relations for earthquake source parameters and magnitudes.
- 995 *Bulletin of the Seismological Society of America*, 66(5), 1501–1523.
- 996 <https://pubs.geoscienceworld.org/ssa/bssa/article/66/5/1501/117604>
- 997 González, Á. (2017). The Spanish National Earthquake Catalogue: Evolution, precision and
- 998 completeness. *Journal of Seismology*, 21(3), 435–471. 10.1007/s10950-016-9610-8
- 999 Guimera, J., & Alvaro, M. (1990). Structure et évolution de la compression alpine dans la
- 1000 Chaîne ibérique et la Chaîne côtière catalane (Espagne). *Bulletin De La Société*
- 1001 *Géologique De France*, 6(2), 339–348. 10.2113/gssgfbull.VI.2.339



- 1002 Hongxing, G., & Anderson, J. K. (2007). Fault throw profile and kinematics of Normal fault:
1003 conceptual models and geologic examples. *Geological Journal of China Universities*,
1004 13(1), 75.
- 1005 Huang, J., Abrahamson, N. A., Sung, C., & Chao, S. (2024). New Empirical Source-Scaling
1006 Laws for Crustal Earthquakes Incorporating Fault Dip and Seismogenic-Thickness
1007 Effects. *Seismological Research Letters*, 95(4), 2352–2367. 10.1785/0220240034
- 1008 Hyndman, R. D., Yamano, M., & Oleskevich, D. A. (1997). The seismogenic zone of
1009 subduction thrust faults. *Island Arc*, 6(3), 244–260. 10.1111/j.1440-
1010 1738.1997.tb00175.x
- 1011 IGN. (2025). *Instituto Geográfico Nacional (2025) Servicio de Información Sísmica*.
- 1012 Jackson, C. A. -, & Rotevatn, A. (2013). 3D seismic analysis of the structure and evolution
1013 of a salt-influenced normal fault zone: A test of competing fault growth models.
1014 *Journal of Structural Geology*, 54, 215–234. 10.1016/j.jsg.2013.06.012
- 1015 Jackson, M. P. A., & Hudec, M. R. (2005). Stratigraphic record of translation down ramps in
1016 a passive-margin salt detachment. *Journal of Structural Geology*, 27(5), 889–911.
1017 10.1016/j.jsg.2005.01.010
- 1018 Jolivet, L., & Faccenna, C. (2000). Mediterranean extension and the Africa-Eurasia
1019 collision. *Tectonics*, 19(6), 1095–1106. 10.1029/2000TC900018
- 1020 Kanamori, H., & Anderson, D. L. (1975). Theoretical basis of some empirical relations in
1021 seismology. *Bulletin of the Seismological Society of America*, 65(5), 1073–1095.
1022 <https://pubs.geoscienceworld.org/ssa/bssa/article/65/5/1073/117458>



- 1023 Kane, K. E., Jackson, C. A. -, & Larsen, E. (2010). Normal fault growth and fault-related
1024 folding in a salt-influenced rift basin: South Viking Graben, offshore Norway. *Journal*
1025 *of Structural Geology*, 32(4), 490–506. 10.1016/j.jsg.2010.02.005
- 1026 Leonard, M. (2010). Earthquake fault scaling; self-consistent relating of rupture length,
1027 width, average displacement, and moment release. *Bulletin of the Seismological*
1028 *Society of America*, 100(5A), 1971–1988. 10.1785/0120090189
- 1029 Leonard, M. (2014). Self-consistent earthquake fault-scaling relations; update and
1030 extension to stable continental strike-slip faults. *Bulletin of the Seismological Society*
1031 *of America*, 104(6), 2953–2965. 10.1785/0120140087
- 1032 Lirer, F., Foresi, L. M., Iaccarino, S. M., Salvatorini, G., Turco, E., Cosentino, C., Sierro, F.
1033 J., & Caruso, A. (2019). Mediterranean Neogene planktonic foraminifer biozonation
1034 and biochronology. *Earth-Science Reviews*, 196, 102869.
1035 10.1016/j.earscirev.2019.05.013
- 1036 Lofi, J. (2011). *Seismic atlas of the "Messinian salinity crisis" markers in the Mediterranean*
1037 *and Black Seas*. Commission for the Geological Map of the World.
- 1038 Maillard, A., Mauffret, A., Watts, A. B., Torné, M., Pascal, G., Buhl, P., & Pinet, B. (1992).
1039 Tertiary sedimentary history and structure of the Valencia trough (western
1040 Mediterranean). *Tectonophysics*, 203(1), 57–75. 10.1016/0040-1951(92)90215-R
- 1041 Maillard, A., & Mauffret, A. (2013). Structure and present-day compression in the offshore
1042 area between Alicante and Ibiza Island (Eastern Iberian Margin). *Tectonophysics*,
1043 591, 116–130. 10.1016/j.tecto.2011.07.007



- 1044 Mansfield, C. S., & Cartwright, J. A. (1996). High resolution fault displacement mapping
1045 from three-dimensional seismic data: evidence for dip linkage during fault growth.
1046 *Journal of Structural Geology*, 18(2), 249–263. 10.1016/S0191-8141(96)80048-4
- 1047 Marsh, N., Imber, J., Holdsworth, R. E., Brockbank, P., & Ringrose, P. (2010). The structural
1048 evolution of the Halten Terrace, offshore Mid-Norway: extensional fault growth and
1049 strain localisation in a multi-layer brittle-ductile system. *Basin Research*, 22(2), 195–
1050 214. 10.1111/j.1365-2117.2009.00404.x
- 1051 Martí, J., Mitjavila, J., Roca, E., & Aparicio, A. (1992). Cenozoic magmatism of the valencia
1052 trough (western mediterranean): Relationship between structural evolution and
1053 volcanism. *Tectonophysics*, 203(1), 145–165. 10.1016/0040-1951(92)90221-Q
- 1054 Martínez-Solares, J. M., & Mezcuá, J. (2002). *Catálogo sísmico de la Península Ibérica*.
1055 Madrid (Spain): Instituto Geográfico Nacional.
- 1056 Maurin, J., & Nivière, B. (1999). Extensional forced folding and décollement of the pre-rift
1057 series along the Rhine graben and their influence on the geometry of the syn-rift
1058 sequences. *Forced Folds and Fractures* (pp. 73–86). The Geological Society of
1059 London. 10.1144/GSL.SP.2000.169.01.06
- 1060 McClusky, S., Reilinger, R., Mahmoud, S., Ben Sari, D., & Tealeb, A. (2003). GPS
1061 constraints on Africa (Nubia) and Arabia plate motions. *Geophysical Journal*
1062 *International*, 155(1), 126–138. 10.1046/j.1365-246X.2003.02023.x
- 1063 Molinaro, M., Leturmy, P., Guezou, J. -, Frizon de Lamotte, D., & Eshraghi, S. A. (2005).
1064 The structure and kinematics of the southeastern Zagros fold-thrust belt, Iran: From
1065 thin-skinned to thick-skinned tectonics. *Tectonics*, 24(3), np–n/a.
1066 10.1029/2004TC001633



- 1067 Morley, C. K., Back, S., Van Rensbergen, P., Crevello, P., & Lambiase, J. J. (2003).
1068 Characteristics of repeated, detached, Miocene–Pliocene tectonic inversion events,
1069 in a large delta province on an active margin, Brunei Darussalam, Borneo. *Journal of*
1070 *Structural Geology*, 25(7), 1147–1169. 10.1016/S0191-8141(02)00130-X
- 1071 NEBOT, M., & GUIMERÀ, J. (2018). Kinematic evolution of a fold-and-thrust belt developed
1072 during basin inversion: the Mesozoic Maestrat basin, E Iberian Chain. *Geological*
1073 *Magazine*, 155(3), 630–640. 10.1017/S001675681600090X
- 1074 Nicol, A., Watterson, J., Walsh, J. J., & Childs, C. (1996). The shapes, major axis
1075 orientations and displacement patterns of fault surfaces. *Journal of Structural*
1076 *Geology*, 18(2), 235–248. 10.1016/S0191-8141(96)80047-2
- 1077 Nissen, E., Ghorashi, M., Jackson, J., Parsons, B., & Talebian, M. (2007). The 2005 Qeshm
1078 Island earthquake (Iran)—a link between buried reverse faulting and surface folding
1079 in the Zagros Simply Folded Belt? *Geophysical Journal International*, 171(1), 326–338.
1080 10.1111/j.1365-246X.2007.03514.x
- 1081 Nissen, E., Tatar, M., Jackson, J. A., & Allen, M. B. (2011). New views on earthquake
1082 faulting in the Zagros fold-and-thrust belt of Iran. *Geophysical Journal International*,
1083 186(3), 928–944. 10.1111/j.1365-246X.2011.05119.x
- 1084 Nocquet, J. -, & Calais, E. (2003). Crustal velocity field of western Europe from permanent
1085 GPS array solutions, 1996–2001. *Geophysical Journal International*, 154(1), 72–88.
1086 10.1046/j.1365-246X.2003.01935.x
- 1087 Nocquet, J. (2012). Present-day kinematics of the Mediterranean: A comprehensive
1088 overview of GPS results. *Tectonophysics*, 579, 220–242. 10.1016/j.tecto.2012.03.037



- 1089 Palano, M., González, P. J., & Fernández, J. (2015). The Diffuse Plate boundary of Nubia
1090 and Iberia in the Western Mediterranean: Crustal deformation evidence for viscous
1091 coupling and fragmented lithosphere. *Earth and Planetary Science Letters*, 430, 439–
1092 447. 10.1016/j.epsl.2015.08.040
- 1093 Pascal, G., Torné, M., Buhl, P., Watts, A. B., & Mauffret, A. (1992). Crustal and velocity
1094 structure of the Valencia trough (western Mediterranean), Part II. Detailed
1095 interpretation of five Expanded Spread Profiles. *Tectonophysics*, 203(1), 21–35.
1096 10.1016/0040-1951(92)90213-P
- 1097 PASCOE, R., HOOPER, R., STORHAUG, K., & HARPER, H. (Jan 1, 1999). Evolution of
1098 extensional styles at the southern termination of the Nordland Ridge, Mid-Norway: a
1099 response to variations in coupling above Triassic salt. Paper presented at the , 5(1)
1100 83–90. 10.1144/0050083 <https://www.lyellcollection.org/doi/10.1144/0050083>
- 1101 Perea, H. (2006). *Falles actives i perillositat sísmica al marge nord-occidental del solc de*
1102 *València*
- 1103 Pérez-Peña, A., Martín-Davila, J., Gárate, J., Berrocoso, M., & Bufo, E. (2010). Velocity
1104 field and tectonic strain in Southern Spain and surrounding areas derived from GPS
1105 episodic measurements. *Journal of Geodynamics*, 49(3), 232–240.
1106 10.1016/j.jog.2010.01.015
- 1107 Ramos, A., Lopez-Mir, B., Wilson, E. P., Granado, P., & Muñoz, J. A. (2020). 3D
1108 reconstruction of syn-tectonic strata in a salt-related orogen: learnings from the Lleret
1109 syncline (South-central Pyrenees). *Acta Geológica Hispanica*, 18(1), 1–19.
1110 10.1344/GeologicaActa2020.18.20



- 1111 Ramos, A., de Ruig, M. J., Pedrera, A., Alfaro, P., & Martin-Rojas, I. (2025). Salt expulsion
1112 triggered by prograding clinoforms in the SW Valencia Trough (SE Spain). *Marine and*
1113 *Petroleum Geology*, 173, 107268. 10.1016/j.marpetgeo.2024.107268
- 1114 Ramos, A., Pedrera, A., García-Senz, J., López-Mir, B., & Salas, R. (2023). Seismic
1115 evidence for ductile necking of the mid-lower crust beneath the Columbrets Basin
1116 (Western Mediterranean). *Terra Nova (Oxford, England)*, 35(5), 404–412.
1117 10.1111/ter.12664
- 1118 Rehault, J., Boillot, G., & Mauiffret, A. (1984). The Western Mediterranean Basin geological
1119 evolution. *Marine Geology*, 55(3), 447–477. 10.1016/0025-3227(84)90081-1
- 1120 Ribó, M., Puig, P., Muñoz, A., Lo Iacono, C., Masqué, P., Palanques, A., Acosta, J., Guillén,
1121 J., & Gómez Ballesteros, M. (2016a). Morphobathymetric analysis of the large fine-
1122 grained sediment waves over the Gulf of Valencia continental slope (NW
1123 Mediterranean). *Geomorphology*, 253, 22–37. 10.1016/j.geomorph.2015.09.027
- 1124 Ribó, M., Puig, P., Urgeles, R., Van Rooij, D., & Muñoz, A. (2016b). Spatio-temporal
1125 evolution of sediment waves developed on the Gulf of Valencia margin (NW
1126 Mediterranean) during the Plio-Quaternary. *Marine Geology*, 378, 276–291.
1127 10.1016/j.margeo.2015.11.011
- 1128 Richardson, N. J., Underhill, J. R., & Lewis, G. (2005). The role of evaporite mobility in
1129 modifying subsidence patterns during normal fault growth and linkage, Halten
1130 Terrace, Mid-Norway. *Basin Research*, 17(2), 203–223. 10.1111/j.1365-
1131 2117.2005.00250.x



- 1132 Roca, E. (1994). La evolución geodinámica de la Cuenca Catalano-Balear y áreas
1133 adyacentes desde el Mesozoico hasta la actualidad. *Acta Geologica Hispanica*,
1134 29(1), 3–25. <https://raco.cat/index.php/ActaGeologica/article/view/75462>
- 1135 Roca, E. (2001). The Northwest Mediterranean Basin (Valencia Trough, Gulf of Lions and
1136 Liguro-Provençal basins): structure and geodynamic evolution. *Mem. Mus. Natl. Hist.*
1137 *Nat. (France)* (pp. 671–706)
- 1138 Roca, E., Frizon de Lamotte, D., Mauffret, A., Bracene, R., Verges, J., Benaouali, N.,
1139 Fernandez, M., Munoz, J. A., & Zeyen, H. (2004). TRANSMED-transect II (Aquitaine
1140 basin, Pyrenees, Ebro basin, Catalan coastal ranges, Valencia trough, Balearic
1141 promontory, Algerian basin, Tell, Sahara Atlas, Sahara platform). In : W. Cavazza, F.
1142 Roure, W. Spakman, G.M. Stampfli and P.A. Ziegler (Eds). The TRANSMED Atlas - the
1143 Mediterranean region from Crust to Mantle. *Springer, Berlin* [https://hal.science/hal-](https://hal.science/hal-00069583)
1144 [00069583](https://hal.science/hal-00069583)
- 1145 Roca, E., & Desegaulx, P. (1992). Analysis of the geological evolution and vertical
1146 movements in the València Trough area, western Mediterranean. *Marine and*
1147 *Petroleum Geology*, 9(2), 167, IN1, 177–176, IN8, 185. 10.1016/0264-8172(92)90089-W
- 1148 Roca, E., & Guimerà, J. (1992). The Neogene structure of the eastern Iberian margin:
1149 Structural constraints on the crustal evolution of the Valencia trough (western
1150 Mediterranean). *Tectonophysics*, 203(1), 203–218. 10.1016/0040-1951(92)90224-T
- 1151 Roca, E., Sans, M., Cabrera, L., & Marzo, M. (1999). Oligocene to Middle Miocene
1152 evolution of the central Catalan margin (northwestern Mediterranean).
1153 *Tectonophysics*, 315(1), 209–229. 10.1016/S0040-1951(99)00289-9



- 1154 Rouby, D., Guillocheau, F., Robin, C., Bouroullec, R., Raillard, S., Castelltort, S., & Nalpas,
1155 T. (2003). Rates of deformation of an extensional growth fault/raft system (offshore
1156 Congo, West African margin) from combined accommodation measurements and 3-
1157 D restoration. *Basin Research*, 15(2), 183–200. 10.1046/j.1365-2117.2003.00200.x
- 1158 Roustaei, M., Nissen, E., Abbassi, M., Gholamzadeh, A., Ghorashi, M., Tatar, M., Yamini-
1159 Fard, F., Bergman, E., Jackson, J., & Parsons, B. (2010). The 2006 March 25 Fin
1160 earthquakes (Iran)—insights into the vertical extents of faulting in the Zagros Simply
1161 Folded Belt. *Geophysical Journal International*, 181(3), 1275–1291. 10.1111/j.1365-
1162 246X.2010.04601.x
- 1163 Ruff, L., & Kanamori, H. (1983). Seismic coupling and uncoupling at subduction zones.
1164 *Tectonophysics*, 99(2), 99–117. 10.1016/0040-1951(83)90097-5
- 1165 Ruig, M. J. d. (1996). Extensional diapirism in the eastern Prebetic foldbelt, southeastern
1166 Spain. *AAPG Memoir*, (65) <https://www.osti.gov/biblio/585188>
- 1167 Sàbat, F., Gelabert, B., Rodríguez-Perea, A., & Giménez, J. (2011). Geological structure
1168 and evolution of Majorca: Implications for the origin of the Western Mediterranean.
1169 *Tectonophysics*, 510(1), 217–238. 10.1016/j.tecto.2011.07.005
- 1170 SALAS, R., GUIMERA, J., MAS, R., MARTIN-CLOSAS, C., MELENDEZ, A., & ALONSO, A.
1171 (2001a). Evolution of the Mesozoic Central Iberian Rift System and its Cainozoic
1172 inversion (Iberian chain). *Mémoires Du Muséum National D'histoire Naturelle* (1993),
1173 186, 145–186.
- 1174 SALAS, R., GUIMERA, J., MAS, R., MARTIN-CLOSAS, C., MELENDEZ, A., & ALONSO, A.
1175 (2001b). Evolution of the Mesozoic Central Iberian Rift System and its Cainozoic



- 1176 inversion (Iberian chain). *Mémoires Du Muséum National D'histoire Naturelle* (1993),
1177 186, 145–186.
- 1178 Seranne, M. (1999). The Gulf of Lion continental margin (NW Mediterranean) revisited by
1179 IBS: an overview. *Geological Society special publication* (pp. 15–36). The Geological
1180 Society of London. 10.1144/GSL.SP.1999.156.01.03
- 1181 Serpelloni, E., Vannucci, G., Pondrelli, S., Argnani, A., Casula, G., Anzidei, M., Baldi, P., &
1182 Gasperini, P. (2007). Kinematics of the Western Africa-Eurasia plate boundary from
1183 focal mechanisms and GPS data. *Geophysical Journal International*, 169(3), 1180–
1184 1200. 10.1111/j.1365-246X.2007.03367.x
- 1185 Sherkati, S., Molinaro, M., Frizon de Lamotte, D., & Letouzey, J. (2005). Detachment
1186 folding in the Central and Eastern Zagros fold-belt (Iran): salt mobility, multiple
1187 detachments and late basement control. *Journal of Structural Geology*, 27(9), 1680–
1188 1696. 10.1016/j.jsg.2005.05.010
- 1189 Soler y José, R., Martínez del Olmo, W., Megías, A. G., & Abeger Monteagudo, J. A. (1983).
1190 Rasgos básicos del neógeno del Mediterráneo español. *Mediterránea. Serie de*
1191 *Estudios Geológicos*, 1, 71–82.
- 1192 STAMPFLI, G. M., & HOCKER, C. F. W. (1989). Messinian palaeorelief from a 3-D seismic
1193 survey in the Tarraco concession area (Spanish Mediterranean Sea). *Geologie En*
1194 *Mijnbouw*, 68(2), 201–210.
- 1195 Stewart, S. A., Ruffell, A. H., & Harvey, M. J. (1997). Relationship between basement-linked
1196 and gravity-driven fault systems in the UKCS salt basins. *Marine and Petroleum*
1197 *Geology*, 14(5), 581–604. 10.1016/S0264-8172(97)00008-1



- 1198 Stich, D., Martín, R., & Morales, J. (2010). *Moment tensor inversion for Iberia-Maghreb*
1199 *earthquakes 2005-2008*. Elsevier.
- 1200 Stich, D., Serpelloni, E., de Lis Mancilla, F., & Morales, J. (2006). Kinematics of the Iberia–
1201 Maghreb plate contact from seismic moment tensors and GPS observations.
1202 *Tectonophysics*, 426(3), 295–317. 10.1016/j.tecto.2006.08.004
- 1203 Stirling, M., Goded, T., Berryman, K., & Litchfield, N. (2013). Selection of earthquake
1204 scaling relationships for seismic-hazard analysis. *Bulletin of the Seismological*
1205 *Society of America*, 103(6), 2993–3011. 10.1785/0120130052
- 1206 Stirling, M., Rhoades, D., & Berryman, K. (2002). Comparison of earthquake scaling
1207 relations derived from data of the instrumental and preinstrumental era. *Bulletin of*
1208 *the Seismological Society of America*, 92(2), 812–830. 10.1785/0120000221
- 1209 Stock, C., & Smith, E. G. C. (2000). Evidence for different scaling of earthquake source
1210 parameters for large earthquakes depending on faulting mechanism. *Geophysical*
1211 *Journal International*, 143(1), 157–162. 10.1046/j.1365-246x.2000.00225.x
- 1212 Thorsen, C. E. (1963). Age of growth faulting in southeast Louisiana.
- 1213 Torné, M., Pascal, G., Buhl, P., Watts, A. B., & Mauffret, A. (1992). Crustal and velocity
1214 structure of the Valencia trough (western Mediterranean), Part I. A combined
1215 refraction/ wide-angle reflection and near-vertical reflection study. *Tectonophysics*,
1216 203(1), 1–20. 10.1016/0040-1951(92)90212-O
- 1217 Tvedt, A. B. M., Rotevatn, A., Jackson, C. A. -, Fossen, H., & Gawthorpe, R. L. (2013).
1218 Growth of normal faults in multilayer sequences: A 3D seismic case study from the



- 1219 Egersund Basin, Norwegian North Sea. *Journal of Structural Geology*, 55, 1–20.
- 1220 10.1016/j.jsg.2013.08.002
- 1221 van Hinsbergen, D. J. J., Torsvik, T. H., Schmid, S. M., Mañenco, L. C., Maffione, M.,
- 1222 Vissers, R. L. M., Gürer, D., & Spakman, W. (2020). Orogenic architecture of the
- 1223 Mediterranean region and kinematic reconstruction of its tectonic evolution since the
- 1224 Triassic. *Gondwana Research*, 81, 79–229. 10.1016/j.gr.2019.07.009
- 1225 van Hinsbergen, D. J. J., Vissers, R. L. M., & Spakman, W. (2014). Origin and consequences
- 1226 of western Mediterranean subduction, rollback, and slab segmentation. *Tectonics*
- 1227 (*Washington, D.C.*), 33(4), 393–419. 10.1002/2013TC003349
- 1228 Vargas, H., Gaspar-Escribano, J. M., López-Gómez, J., Van Wees, J., Cloetingh, S., de La
- 1229 Horra, R., & Arche, A. (2009). A comparison of the Iberian and Ebro Basins during the
- 1230 Permian and Triassic, eastern Spain: A quantitative subsidence modelling approach.
- 1231 *Tectonophysics*, 474(1), 160–183. 10.1016/j.tecto.2008.06.005
- 1232 Verges, J., & Sabat, F. (1999). Constraints on the Neogene Mediterranean kinematic
- 1233 evolution along a 1000 km transect from Iberia to Africa. *Geological Society special*
- 1234 *publication* (pp. 63–80). The Geological Society of London.
- 1235 10.1144/GSL.SP.1999.156.01.05
- 1236 Verges, J., & Fernandez, M. (2012). Tethys–Atlantic interaction along the Iberia–Africa
- 1237 plate boundary: The Betic–Rif orogenic system. *Tectonophysics*, 579, 144–172.
- 1238 10.1016/j.tecto.2012.08.032
- 1239 Wells, D. L., & Coppersmith, K. J. (1994). New empirical relationships among magnitude,
- 1240 rupture length, rupture width, rupture area, and surface displacement. *Bulletin of the*



- 1241 *Seismological Society of America*, 84(4), 974–1002.
- 1242 <https://pubs.geoscienceworld.org/ssa/bssa/article/84/4/974/119792>
- 1243 Weng, H., & Yang, H. (2017). Seismogenic width controls aspect ratios of earthquake
- 1244 ruptures. *Geophysical Research Letters*, 44(6), 2725–2732. 10.1002/2016gl072168
- 1245 Withjack, M. O., & Callaway, S. (2000). Active normal faulting beneath a salt layer; an
- 1246 experimental study of deformation patterns in the cover sequence. *AAPG Bulletin*,
- 1247 84(5), 627–651. 10.1306/C9EBCE73-1735-11D7-8645000102C1865D
- 1248 Withjack, M. O., Olson, J., & Peterson, E. (1990). Experimental models of extensional
- 1249 forced folds. *AAPG Bulletin*, 74(7), 1038–1054. 10.1306/0C9B23FD-1710-11D7-
- 1250 8645000102C1865D
- 1251 Yen, Y., & Ma, K. (2011a). Source-scaling relationship for M 4.6–8.9 earthquakes,
- 1252 specifically for earthquakes in the collision zone of Taiwan. *Bulletin of the*
- 1253 *Seismological Society of America*, 101(2), 464–481. 10.1785/0120100046
- 1254 Yen, Y., & Ma, K. (2011b). Source-scaling relationship for M 4.6–8.9 earthquakes,
- 1255 specifically for earthquakes in the collision zone of Taiwan. *Bulletin of the*
- 1256 *Seismological Society of America*, 101(2), 464–481. 10.1785/0120100046
- 1257 Zazo, C. (1979). El problema del límite Plio-Pleistoceno en el litoral S y SE de España.
- 1258 *Trabajos N/Q*, 9, 65–72.
- 1259
- 1260
- 1261